Numerical Analysis of Nitrogen Oxides in Turbulent Lifted H_2/N_2 Cabra Jet Flame Issuing Into a Vitiated Coflow

Bahamin Bazooyar [a,b,*], Ahmad Shariati [a], Mohammadreza Khosravi-Nikou [a,c], Seyed Hassan Hashemabadi [d]

[a] *Ahvaz Faculty of Petroleum, Petroleum University of Technology (PUT), Ahvaz, P.O. Box 6198144471, Iran*

[b] *Department of Design & Engineering, School of Creative Arts and Engineering (CAE), Staffordshire University, Stoke-on-Trent, ST4 2DE, United Kingdom*

[c] *Abadan Institute of Technology, Petroleum University of Technology (PUT), 63156 ,Abadan, Iran*

[d] *School of Chemical Engineering, Iran University of Science and Technology (IUST), 16846-13114, Tehran, Iran*

[1,*] Corresponding author: Bahamin Bazooyar, Research Fellow in Turbulent Combustion (b.bazooyar@staffs.ac.uk); Tel: +44 73 05 34 15 05, Fax: +44 17 82 29 58 62

[2] Ahmad Shariati, Associate Professor of Chemical Engineering, (Shariati@put.ac.ir)

[3] Mohammadreza Khosravi-Nikou, Associate Professor of Chemical Engineering, (mr.khosravi@put.ac.ir)

[4] Seyed Hassan Hashemabadi, Professor of Chemical Engineering, (hashemabadi@iust.ac.ir)

ABSTRACT: This paper gives an in-depth insight into NO_X (NO, NO_2, and N_2O) formation of H_2/N_2 turbulent Cabra jet flame issuing into a hot vitiated coflow. The joint composition probability density function (PDF) was employed to model the combustion and to specify the characteristics of the flame (i.e., scalar variables, concentration of species etc.). The turbulent transport term was modelled by Reynold-Average-Naiver-Stokes (RANS) SSG and molecular mixing was modelled by modified curl model. A combustion mechanism including 13 species and 34 reactions was employed to define the thermochemical state of the flame. The chemical reaction terms were resolved and accelerated by In Situ Adaptive Tabulation (ISAT). The simulation was performed at different equivalence ratios (ER), fuel jet nitrogen content ($Y_{N_2,C}$), coflow (T_C) and jet temperatures (T_J), coflow oxygen ($Y_{O_2,C}$) and water contents ($Y_{H_2O,C}$). Results reveal NO_X is composed of 30% NO_2 and 70% NO in the burner. Reaction rate analysis at different operating points in the ignition kernel demonstrates that $N + OH \rightarrow NO + H$ and $NO_2 + H \rightarrow NO + OH$ are dominant reactions in NO formation, while $NO + HO_2 \rightarrow NO_2 + OH$ is the main reaction in NO_2 formation.

Keyword: NO_X, H_2/N_2 Lifted flames, Autoignition, Cabra flame, Flameless combustion

1. Introduction

Hydrogen, the lightest and the most abundant component in the cosmos [1], is a highly combustible gas at the standard conditions that ignites at a very wide range of concentrations-from 4% to 75% (by volume) in air [2]. While the source of pure hydrogen is limited on earth, it has been given considerable attention as a renewable fuel because it is free from carbon and carbon monoxide (CO), carbon dioxide (CO_2), and unburned hydrocarbons (UHC) [3]. Hydrogen can be produced from both renewable and non-renewable sources [4]. This makes it a great potential fuel for the future. Currently, the extraction, utilization, and transition of hydrogen as a fuel is limited due to its specific characteristics. Hydrogen specific physical properties including short ignition delay time, wide flammability range, high diffusivity, high laminar flame speed, and high production costs create the explosion hazard risks in processing plants, seriously limiting the application of hydrogen [5, 6].

Another drawback worthy of further investigation is the potential of this fuel to increase the NO_X as the temperature of hydrogen flame is usually high.

To mitigate the problems associated with the use of hydrogen, it is currently used as an additive to hydrocarbon fuels. In the form of mixture with other hydrocarbon fuels, hydrogen is able to vary the chemical structure of the flame by increasing the reactivity of hydrocarbon fuel, flame stability [7], flame luminosity, heat radiation [8], adiabatic flame temperature, laminar burring velocity [9], and extension of the lean flammability of hydrocarbon fuel [10], shortening of the combustion time, reduction the flame length [11], lifting the flame upstream [12], changing the flame shape [13] (creation of a shorter narrowed blue flame and a central highly luminous yellow plume extending above the visible blue zone [14]), combustion temperature and suppressing the formation of soot [15], decreasing unburned hydrocarbons [16], enhancing stabilization [17], and if carefully managed reducing the NO_X emission [18]. Hydrogen as an additive may also have a negative influence on the combustion by increasing the diffusion of the un-burnt fuel through the flame front [19], resulting in significant NO_X formation [20].

Because of hydrogen high adiabatic flame temperature, hydrogen turbulent jet flames have a great potential for thermal NO formation. Although NO_X could be reduced by the use of it in a very lean mixture with inert or other fuel, this strategy may lead to some serious combustion problems such as flashback [21], flame instability, and poor combustion characteristics. Therefore, one important concern in the use of hydrogen as a fuel additive in turbulent non-premixed flames is to increase its content whilst, maintain the NO_X in an acceptable level. Whether the hydrogen could impact the NO_X is matter of debate because available data are scarce, diverse and somewhat contradictory. Rortveit et al. [22] stated that hydrogen in only the low-NO_X burners can influence the NO_X emission and it has a negligible impact on NO_X in other burners.

NO_X in hydrogen turbulent flames is the subject matter of several studies in the literature. Prediction [23], reduction [24], and characterization of NO_X [25-30] are the most studied topics in hydrogen flames. The existence of NO_X in mixing zone of the hydrogen flames decrease the ignition delay and

brings about early autoignition [31]. In most of turbulent flames, the evolution of NO is highly similar to the evolution of the turbulent structure, being thin near the nozzle and broad at the flame tips [32]. In contrast to other hydrocarbon flames, thermal NO could not be the main NO constituent in turbulent N_2/H_2 flame [33] and other H_2 hybrid flames. Drake and Blint [34] claimed that the main NO formation mechanism in laminar diffusion $CO/H_2/N_2$ hybrid flame depends on flame stretch. They have reported that thermal NO is the main mechanism in the low stretched hydrogen flame. For high stretched flames, N_2O pathway mechanism plays the main role. Other reports also signify the N_2O pathway, and NNH route as the main mechanisms in turbulent hydrogen flames [35, 36]. NO_2 is also reported to form mostly in flame lean areas.

NO_X emission in turbulent non-premixed hydrogen flames is contingent upon several factors including turbulent intensity [37, 38], velocity of coaxial air [39], flame stretch, extinction strain rate [40], flame swirl intensity [41], acoustic properties of air jet [42, 43], recirculation zone properties, equivalence ratio (or excess air [44]), non-equilibrium chemistry HO_2/H_2O_2 [45], flame length, secondary air mixing, Reynold number, residence time of the recirculated gas, temperature, velocity of gaseous combustion products [46], heat radiation and buoyancy [47]. Han et al. [48] have demonstrated that turbulent intensity decreases the thermal NO, whilst leads to more NO_2 formation in turbulent hydrogen diffusion flames. Simulating the non-premixed H_2 turbulent jet flame using the conditional moment cloture (CMC), Smith et al. [49] showed that NO_X is scaled by the residence time of the fume in the combustion chamber with a 1/2 power dependence to fuel jet velocity. They pointed out that in hydrogen flames super-equilibrium H, O and OH species, and sub-equilibrium local flame temperatures decay towards equilibrium downstream of their fuel nozzle. Barlow et al. [50] compared the capability of turbulence-chemistry submodels PDF and CMC in prediction of NO in a diluted hydrogen jet flame, revealing the underestimation of these two submodels in prediction of NO. Moon [51] has revealed that the $EINO_X$ scaling parameter based on the self-similarity is not valid in coaxial air flames because coaxial air breaks down the self-similarity law of flames by changing mixing mechanism.

As an additive, hydrogen may influence the NO_X formation in turbulent flames. Gao et al. [52], using Eddy Dissipation Concept (EDC), have numerically shown that hydrogen plays a vital role in NO_X of turbulent diffusion methane flames and any decrease in fuel hydrogen content leads to the significant NO_X reduction. Kim et al. [44] reported an increase in NO_X using hydrogen. They have also stated that the influence of hydrogen on NO_X could be reduced by increasing excess air and swirl intensity. Yu et al. [53] demonstrated that in flameless mode, hydrogen as an additive of methane does not change the NO_X emission. Kashir et al. [54] numerical simulation based on RANS/PDF and pre-tabulation of methane combustions chemistry using the flamelet concept showed that addition of hydrogen in the Sydney swirl burner thickens the reaction zone, shifts the axial peak temperature towards the nozzle injection plane, and a mild reduction in NO_X emission. Hwang et al. [55] found that turbulent intensity reduces NO_X emission of turbulent nonpremixed H_2/Air jet flames in the upstream region by increasing the strain rate and in the downstream region by enhancing mixing effect.

The fundamental study of NO_X in practical burners can provide significant workable pathways for regulation and management of this gaseous pollutants as well as better understanding the chemistry of hydrogen flames. Because the stabilization in turbulent flames of real burners is maintained by recirculation of hot combusted products with fresh reactants, such a study would be extremely challenging. Cabra jet flame was designed [56] to imitate the environment of non-premixed jet flames by providing a simple case of turbulent reacting flow within a hot environment with low oxygen concentrations. This burner demonstrates several characteristics of real combustion devices by imitating the conditions of advanced combustors. One of the most strongest advantages of this burner is to change the combustion parameters when the chemical kinetics is completely separated from the fluids flow [57]. This feature makes this possible to independently change the combustion variables and investigate the combustion in a highly reactive turbulent flow when it is decoupled from the combustion chemistry.

The lifted turbulent jet flames in a vitiated coflow have been analyzed both experimentally and numerically by many researchers. Gordon et al. [58] gathered an experimental repository of data including temperature, OH and CH_2O mass fractions of this flame. The turbulence structure [59], autoignition [60], flame stabilization [61], flame structure [62], swirls dynamics, visualization [63], the micro-scales structures and the turbulence intensity distribution in the flame [64], sensitivity of preflame zone [65], ignition/extinction [66] of lifted H_2/N_2 jet flame issuing into vitiated coflow have also been extensively studied during the last decade. However, there are rare clues regarding nitrogen chemistry of this flame. What would be the effect of hydrogen in the formation of nitrogen oxides in real burners could be easily found out in the Cabra flame. Since this flame shows many features and characteristics of the combustion in real burners, the fundamental study of nitrogen chemistry may provide significant clues about NO_X in the hydrogen turbulent combustion. Although the autoignition temperature of hydrogen is around 500 ºC [67], the dilution of H_2 with nitrogen may intensify the NO_X formation.

The occurrence of the combustion brings about a sharp temperature gradient in small thickness called flame front. The temperature here is close to the adiabatic flame temperature, thereby leading to significant formation of nitrogen oxides. Even though the flameless combustion could effectively supress sharp gradients of temperatures and species mass fractions by propagating the onset of reactions through a capacious environment, the dilution of H_2 with a large ballast of nitrogen may lead to noticeable significant formation of the nitrogen oxides, while it still maintains the stability of firing. The study of nitrogen oxides around the flame stabilization area could provide clues about the formation of this deleterious combustion pollutants. This document is to analyze the formation of nitrogen oxides with the onset of the autoignition. Another objective is to verify the effect of parameters on the chemistry of nitrogen, and scalar variable. To this end, the modelling of the combustion has been performed, verified, and validated with experimentations. Afterwards, the influence of coflow and jet temperature, oxygen and water content in coflow, and nitrogen and hydrogen content of the fuel jet on the nitrogen structure of turbulent flame is investigated using the

evolution and rate of relevant elementary reactions taking place in proximity of the flame kernel to downstream of fuel nozzle. The transported PDF scalar equations were solved for the species considering its accuracy over conventional methods for handling the chemistry during the turbulent combustion [68].

2. Simulation

This section of the paper describes the burner, computational domain, governing equations, and numerical techniques used in the simulations. Finally, it gives the method used to check the accuracy and validity of the simulation.

2.1 Test case

Cabra et al. [69] designed a jet in a hot coflow (JHC) burner (Fig 1) to imitate the combustion in real burners. The advantage of this burner is that the injection conditions of reactants and hot products could be fully determined, while it emulates the combustion in real burners with recirculation zone. The combustion initiates as a result of the fuel jet moving coaxially with a hot coflow stream coming from the combustion of a lean premixed H_2 flame. The burner has a nozzle with inner diameter D=4.57 mm and stainless-steel wall with thickness W=0.89 mm. The fuel jet nozzle is at the center of a perforated disc. The disc creates a uniform hot vitiated coflow around the H_2/N_2 jet. The diameter of the perforated disk is 210 mm which is large enough to hamper any entrainment by the flame and isolate it for axial locations up to the z/D=25.

2.2 Computational domain

An axisymmetric two-dimensional computational domain is created for simulation of the half of the flame (Fig 2). The domain length and wideness are equal to 50 and 25 times of the jet diameter (D), respectively. It contains unstructured grids in two blocks: one with finer size near the burner central axis, and the other with coarser far from the axis. The results were analyzed by a cylindrical coordinate (r, z) which was considered with an origin at the center of the jet exit plane.

2.3 Boundary conditions

The boundary conditions are: 1) at the upper side and on the right side of the computational domain, the conditions are set to pressure outlet and axis of symmetry, respectively, 2) the walls at the left hand side of the computational domain are defined with thickness of 0.89 mm, density of 8030 kg/m3, specific heat of 502.48 [J. kg^{-1}. K^{-1}], thermal conductivity of 16.27 [W. m^{-1}. K^{-1}] and stainless-steel material. The inlet velocity profiles and rms fluctuations are extracted from the Masri et al. [70] work. Autocorrelation function is used to give the velocity covariance. It is assumed to be linear from 0 to 0.4 between the $0 \le r/R \le 1$ (R is the nozzle radius) and 0.4 and 0 for $1 \le r/R \le 2.87$ and $2.87 \le r/R$, respectively. The uncertainties of measurements are also required to be verified as they could have noticeable influence on the results. These uncertainties for the temperature and the composition of species are 3% and 10%, respectively [71].

2.4 Chemical reactions

The combustion mechanism of Li et al. [72] was employed to handle the combustion chemistry which is an up-to-date version of Muller mechanism [73]. This mechanism includes 15 species (H_2, H, O_2, O, OH, HO_2, H_2O_2, H_2O, and N_2) and 21 elementary chemical reactions. The scheme of this mechanism is represented in table 1 (R1-R19). The accuracy of the Li mechanism in determining the hydrogen chemistry of the Cabra flame was authenticated by Cao et al. [74]. The reactions R20-32 were considered along with the Li combustion mechanism. This sequence includes the formation of NO from thermal and N_2O pathways. Thermal NO is important for this flame as the temperature is enough for ignition and reactions among the combustion species. N_2O pathway is also an important NO formation mechanism at moderate temperatures [75, 76]. The prompt NO is absent as no hydrocarbon radical exists in hydrogen combustion. NO_2 is also kinetically limited to low temperatures and form mostly from reaction between NO and HO_2 and partly from NO, H and O reactions [77]. The complete reaction path of nitrogen oxides is given in Fig 3.

2.5 Governing equations

The RANS-PDF strategy was utilized to solve the governing equations and simulate the turbulent combustion of N_2/H_2 flame. In the finite volume part, the Reynold-Average-Navier-Stoke (RANS) equations is employed to balance the mass, momentum, and energy. A modelled transport equation for the PDF of scalar properties of ensemble notional particles representing the composition of gaseous species is also numerically solved. The required Reynold-stress term ($\overset{\frown}{u_i''u_j''}$) in Navier-Stokes is unclosed at the second moment [78] and is modelled using the following equation:

$$\frac{D}{Dt}(\langle\rho\rangle\overset{\frown}{u_i''u_j''}) = \frac{\partial}{\partial x_k}\left(\langle\rho\rangle\frac{\upsilon_t}{\sigma_k}\frac{\partial\overset{\frown}{u_i''u_j''}}{x_k}\right) + \langle\rho\rangle P_{ij} + \langle\rho\rangle\phi_{ij} - \langle\rho\rangle\delta_{ij}\frac{2}{3}\varepsilon \quad (1)$$

where P_{ij} is the production term of Reynolds stress and is given by:

$$P_{ij} = -\overset{\frown}{u_i''u_k''}\frac{\partial\overset{\circ}{u_j''}}{\partial x_k} - -\overset{\frown}{u_j''u_k''}\frac{\partial\overset{\circ}{u_i''}}{\partial x_k} \quad (2)$$

The pressure-strain term Φij is closed using the Speziale, Sarkar, and Gatski (SSG) model. The coefficient of rapid part of pressure strain correlation is deemed quadratically non-linear [79]:

$$\begin{aligned}\phi_{ij} &= -\left(C_1\rho\varepsilon + C_1^*P\right)b_{ij} + C_2\rho\varepsilon\left(b_{ik}b_{kj} - \frac{1}{3}b_{mn}b_{mn}\delta_{ij}\right) + \left(C_3 - C_3^*\sqrt{b_{ij}b_{ij}}\right)\rho k S_{ij} \\ &+ C_4\rho k\left(b_{ik}S_{jk} + b_{jk}S_{ik} - \frac{2}{3}b_{mn}S_{mn}\delta_{ij}\right) + C_5\rho k\left(b_{ik}\Omega_{jk} + b_{jk}\Omega_{ik}\right)\end{aligned} \quad (3)$$

The coefficients of rapid part of pressure strain correlation are nonlinear. The $k = \frac{\overset{\frown}{u_i''u_i''}}{2}$ and ε are turbulent kinetic energy and its dissipation rate. The normalized Reynold stress anisotropy tensor bij, mean rate of strain and mean rate of rotation Ω_{ij} are given by

$$b_{ij} = \frac{\overset{\frown}{u_i''u_j''}}{2k} - \frac{1}{3}\delta_{ij},\ S_{ij} = \frac{1}{2}\left(\frac{\partial\overset{\circ}{u_i}}{\partial x_j} + \frac{\partial\overset{\circ}{u_j}}{\partial x_i}\right),\ \Omega_{ij} = \frac{1}{2}\left(\frac{\partial\overset{\circ}{u_i}}{\partial x_j} - \frac{\partial\overset{\circ}{u_j}}{\partial x_i}\right) \quad (4)$$

The transport equation for ε (dissipation rate) is modelled via the following equation:

$$\frac{D\langle\rho\rangle\varepsilon}{Dt} = \frac{\partial}{\partial x_j}\left(\langle\rho\rangle\left(\upsilon + \frac{\upsilon_t}{\sigma_\varepsilon}\right)\frac{\partial\varepsilon}{x_j}\right) + \langle\rho\rangle C_{\varepsilon 1}\frac{P_{kk}}{2}\frac{\varepsilon}{k} - \langle\rho\rangle C_{\varepsilon 2}\frac{\varepsilon^2}{k} \quad (5)$$

υ_t is the turbulent viscosity and is defined by:

$$\upsilon_t = C_\mu \frac{k^2}{\varepsilon} \qquad 6$$

Table 2 lists the constants for turbulent model equations which are used to improve the spreading and decaying rates. The PDF/ Particle composition strategy was employed to model the transport of composition PDF [80]:

$$\frac{D}{Dt}\left(\langle\rho\rangle \tilde{f}_\phi\right) + \frac{\partial}{\partial \psi_k}\left(\langle\rho\rangle S_K \tilde{f}_\phi\right) = -\frac{\partial}{\partial x_i}\left(\langle\rho\rangle\langle u_i''|\psi\rangle \tilde{f}_\phi\right) + \frac{\partial}{\partial \psi_k}\left(\langle\rho\rangle\left\langle \frac{1}{\rho}\frac{\partial J_{i,k}}{\partial x_i}\middle|\psi\right\rangle \tilde{f}_\phi\right) \qquad 7$$

The closure problem is seen on right hand side of the Eq.7 and thus modeling is required. The first term represents turbulent scalar flux, which is transport resulting from the turbulent velocity fluctuations in physical space and can be modelled using gradient-diffusion model:

$$\langle\rho\rangle\langle u_i''|\psi\rangle \tilde{f}_\phi = -\Gamma_T \frac{\partial \tilde{f}_\phi}{\partial x_i} \qquad 8$$

in which Γ_T indicates the turbulent viscosity. The term $\frac{\partial}{\partial \psi_i}\left(\langle\rho\rangle S_K \tilde{f}_\phi\right)$ is the molecular flux transport in compositional space and refers to micro-mixing term. In this article, the micro-mixing is modelled with the modified curl model (C_ϕ) [81].

For this flame, change of energy in control volume is equal to energy transfer due to conduction, species diffusion, viscous dissipation and heat of chemical reactions. The following energy equation is also required:

$$\frac{\partial}{\partial x_i}\left(\langle\rho\rangle E\right) + \nabla.\left(\vec{\upsilon}\left(\langle\rho\rangle E + p\right)\right) = \nabla.\left(k_{eff}\nabla T - \sum_j h_j \vec{J}_j + \left(\bar{\bar{\tau}}_{eff}.\vec{\upsilon}\right)\right) + S_h \qquad 9$$

where k_{eff} indicates the effective conductivity ($k+k_t$) and $\vec{J_j}$ denotes the diffusion flux of species.

The heat sources resulted from the particle radiation is modelled from the following equation:

$$-\nabla.q_r = -4\pi\left(a\frac{\sigma T^4}{\pi} + E_p\right) + \left(a + a_p\right)G \qquad 10$$

where q_r is the radiation flux, a and a_p is the absorption coefficient and particle equivalent absorption coefficient, E_p is the equivalent emission of particles, σ is scattering coefficient, and G is the incident

radiation. This radiation is modelled based on the expansion of radiation intensity into an orthogonal series of spherical harmonies [82]. The modeling of flame radiation is essential for accurate prediction of NO_X emission [83], especially in hydrogen flames [84] with high temperature. Thermal effect is mainly responsible for the radiation in hydrogen flames [85]. Frassoldati et al. [86] have shown that reactions $NO_2+H_2 \rightarrow HONO+H$ and $N_2H_2+NO \rightarrow N_2O+NH_2$ increase the predictability of numerical simulation for NO_x emission.

2.6 Numerical method

The hybrid algorithm of finite volume PDF/particle is used to solve the governing equations. A steady segregated solver with implicit formulation is exploited in the finite volumes. The flow characteristics including mean fluid velocity, turbulent viscosity and turbulent timescale are obtained from the finite volumes and then are used in the PDF/particle algorithm. The mean density and viscosity are calculated from the properties of particle and implemented in the equation of motion. A second order upwind method is utilized for the space derivatives of the advection terms in the transport equations. The PREssure Staggering Option (PRESTO) and the Pressure Implicit with Split Operator (PISO) are utilized for pressure and pressure coupling, respectively. A particle-based Lagrangian method designed by professor Pope [87] is employed for solving the evolution of PDF equations. This technique is more time efficient than the convectional discretization methods since it leads to the linear increase of the computational cost with number of grid points rather than exponential. In the Lagrangian particle-based method, the properties of an ensemble of particles evolve statistically in physical and composition spaces based on stochastic differential equations. Thus, the ensemble PDF of the particles is statistically equivalent to PDF obtained from the modelled joint composition PDF equation. A weak point of the Monte Carlo strategy is that the statistical errors, which results from the finite number of particles, N representing the joint PDF, diminishes only with $N^{-1/2}$. This problem can be solved by averaging the ensemble PDF of the particles in temporal space. Mass weighted average of temperature, O_2, N_2 mass fractions are also area-averaged and monitored at the exit plane of domain. The governing equations were numerically discretized and solved for the

defined two-dimensional statistically axisymmetric domain with the boundary conditions given in table 3.

The verification of the numerical simulation was also performed for different numbers of grids (12, , 38, 50, and 100 k). Preliminary simulations showed that the sensitivity of results on the number of grids disappear with 37 thousand cells, leading to 1% or fewer relative error in mean temperature and concentrations of species. In the verification of the solution, the impact of particles number in each cell N_{pc} was also considered. The number of particles N_{pc}=50 was considered optimum as the sensitivity of the obtained results in terms of mean temperature and mean mass fraction of major species was less than 1%.

2.7 Accuracy of simulations

A comparison between the simulated and experimented results was performed in terms of temperature, mixture fraction, and OH, O_2 and N_2 mass fraction to rest assured that NO is accurately simulated. Axial diffusion was not a part of simulation as the convection term is dominant. Hence, a mixture fraction based on the trace of argon seems quite reasonable:

$$\xi = \frac{Y_{Ar}}{Y_{Ar,fuel}} \qquad 11$$

where Y_{Ar} and $Y_{Ar,fuel}$ indicate spatial argon mass fraction and its initial values in the fuel jet. The mass fraction of argon in the fuel jet was considered 10^{-6}. This definition of mixture fraction is adequate since effects of differential diffusion are not considered in the model.

The validation of mixture fraction (Fig 4) gives the accuracy of the simulations in mixing field. Accurate prediction of mixing fields is dependent on the employed turbulent model. A reliable turbulent model which is accurate not only in upstream of flame, but also in downstream of flame is required, especially for this test since the flame is lifted and the evolution of thermal NO is shown well.

3. Result and discussion

The computational domain was partitioned in thirty-six parts for efficient parallel processing using 36 CPU cores in LINUX small cluster. The code is optimized in three stages. First, the simulation

was run for fluid mechanics and turbulence without any reactions and PDF equations. At the second stage, the stochastic particle tracking of joint PDF composition for species was considered without any chemical reactions in the computational codes. At the final stage, gaseous chemical reactions entered the simulation to obtain the spatial concentrations of species.

3.1 Validation

The results are verified via comparison of simulation with experimental data (Fig 4). The measurements are available for (run 1 in table 4-flame lift-off: z/D=10) [70]. For this flame, the simulation and measurements could be compared for cases with a same flame lift-off length [74]. The run 1 (table 4) with T_C=1045 K matches exactly that of Cabra et al. [69] leading to the same flame lift-off height z/D=10. This flame lift-off height in the simulations was obtained from local OH mass fractions. For this flame, the OH mass fraction is the marker of autoignition. Cabra et al. [69] stated that the measured OH mass fractions goes up to the 2×10^{-4} at the visible region of the flame base. The flame lift-off height was considered the closest distance to the fuel nozzle in the axis of the flame where the OH mass fraction reaches 2×10^{-4}.

The turbulence mixing is validated by comparison of experimental and simulation results in terms of the mean mixture fraction. The issue of mixing in the simulations is handled by the applied turbulence model. The results are well accurate for low axial locations, although losing their precision downstream of the fuel nozzle for high axial locations. This different precision in simulation results are due to the application of the RANS modelling which lose their accuracy in presenting the characteristics of the flow downstream of free shear jets. The k-ε turbulence model was also compared with SSG model by other researchers [70, 74]. Their results indicate that even the modified versions of k-ε fail to predict the local turbulence mixing downstream of the turbulent jet.

The radial and axial profiles of oxygen (O_2), nitrogen (N_2), water (H_2O) and oxygen hydroxide (OH), temperature were compared with experiments to add more confidence in simulations for nitrogen oxides. The accuracy of simulation in giving the spatial temperatures, jet spreading, mixing, and the reactive zone is confirmed. Since the temperature of reactive flow in the burner (@1550 K)

is on a par of hydrogen flameless combustion (@ 1600 K [53, 88]), the combustion takes place in this burner without appearance of visible flame. The error of experiments in the graphs were temperature, 1%; N_2, 3%; H_2O; 6%; OH, 10%; and mixture fraction, 6%.

The nitrogen oxides NO, NO_2, and N_2O are analyzed at different operating conditions. The rate of reactions is also analyzed at the ignition kernel. This analysis provides accurate results in terms of sensitivity and comprehensiveness, as the transported PDF Scalar has the advantage of calculating nonlinear chemical elementary reactions without any approximation, the fact that was previously authenticated in capturing the strong sensitivity of flame lift-off height to combustion parameters [58, 70, 74, 89]. Considering the statistical nature of turbulence, the concentrations of species and as a result instantaneous reaction rates includes strong fluctuations, the least square smoothing filter was employed to smooth out the fluctuations and noisy results of instantaneous reaction rates [90].

3.2 NO_X formation: influence of parameters

3.2.1 Coflow temperature

Fig 5 shows the contour of the nitrogen oxides mean mass fractions at different coflow temperatures 1030, 1045, 1060, and 1080 K. It is notable that small variations in the coflow temperature could change the level of nitrogen oxides. The coflow temperature has a significant impact on the level of NO, NO_2 and N_2O. The overall shape of NO contour remains the same for all the verified coflow temperatures. However, NO_2 contour shape strongly depends on the 50 K variations in temperature. The threshold of the N_2O formation shifts toward the fuel nozzle.

Comparing the contour plots of nitrogen oxides (especially NO and NO_2) and OH mass fractions (not shown here), the nitrogen oxides (NO, NO_2) evolves much closer to the nozzle than the flame itself. Whether the nitrogen oxides form within either the thermal runaway or radical build-up state need more intrusive inspection with unsteady turbulence modeling. Fig 5 confirms that the NO and NO_2 forms during initial confrontation of the coflow and fuel jets even closer than. Considering flame lift-off height (Z/D=15-20) for range of investigated coflow temperatures, the evolution of nitrogen oxides begins closer compared to than OH radicals [91]. The reasons that can be given for this rapid

NO evolution during autoignition of N_2/H_2 are the high concentrations of the nitrogen in the fuel jet and close spatial temperatures over the entire flame. Since the concentrations of species in vitiated coflow flames are in equilibrium, there is potential for NO to form in coflow and also to penetrate the turbulent hydrogen and nitrogen jet leading to this rapid evolution of nitrogen species. This phenomenon was observed for NO and NO_2. However, contour plots of Fig 5 demonstrate that the nitrous oxide evolves after the ignition kernel and lift of the flame.

Analysis of the elementary reactions along the flame axis provides reliable clues about the dominant chemical reaction at the flame downstream and upstream. The contour plots of Fig 5 show that the maximum level of nitrogen oxides corresponds to the axis of the flame after the beginning of ignition. Therefore, the contribution of each elementary reaction in the consumption and production of NO, NO_2 and N_2O is discussed near the flame kernel to find the dominant reaction in the formation of NO emission for the investigated coflow temperatures. The contribution of elementary reactions reported here are in the unit mol. $cm^{-3}.s^{-1}$ (in figs). The preliminary results have shown that rate of the following reactions in NO formation:

$$N + O_2 \rightarrow NO + O \quad \text{R21}$$

$$N + OH \rightarrow NO + H \quad \text{R22}$$

$$NO_2 + H \rightarrow NO + OH \quad \text{R32}$$

The reactions R20 (backwards) and R21 are the so-called thermal mechanism. The main thermal NO reaction is the backward of R20 by which the nitrogen molecules dissociate and reacts with atomic oxygen. This reaction is the beginning of the thermal NO reaction. However, its rate is significantly lower than reactions above (R21, R22 and R32), thereby contributing negligibly into the total NO and is not analyzed here. NO could also form through other reactions including R25 and R31. However, the rate of these reactions is comparatively lower than the R21, R22, and R32.

The destruction of NO is mainly from:

$$N + NO \rightarrow N_2 + O \quad \text{R20}$$

in which the unstable NO and N atoms react forming the N_2 molecules. This reaction is a part of thermal mechanism for NO. Other reactions including R23, R29, and R30 have negligible participation in the destruction of NO having rate of reactions significantly lower than R20.

In sum, the spatial evolution of R21, 22, and 32 reactions were considered for the formation of NO and the R20 for the destruction of NO because the rates of these reactions are noticeably higher than their counterparts contributing in the formation and destruction of NO. The NO formation from the N_2O (R25) was also separately analyzed to show the comparative role of thermal and N_2O pathway mechanisms.

Fig 6-a gives the spatial evolution of the contribution of elementary reactions to the production and consumption of the nitrogen monoxide. This figure reveals that the main competence for the NO formation exists among the R32 and R22. Depending on the coflow temperature, the dominant reaction in the production of nitrogen monoxide can be either the R22 (@ 1080) or R32 (@ 1045). The R22 is a chain branching reaction occurring between the OH and N radicals. Preceding the thermal runaway, the OH radicals were built up in the induction phase by reaction (R11) near the flame base and take part in the ignition process, thereby forming a clement environment for the chain branching reaction R22. The R32 chain branching reaction takes place between the H radicals and NO_2. In the proximity of the flame kernel where the autoignition begun and as a result the temperature rocketed, the NO_2 becomes highly unstable and there is a great potential for any previously formed NO_2 to vanish in destruction by the main ignition species such H radicals. At higher coflow temperature (1080 K), there is a high likelihood for the destruction of nitrogen dioxide. Therefore, the rate of R32 reaction becomes significantly lower and its contribution in NO disappears.

Fig 6-b gives the spatial evolution of the R29, R30, and R31. These reactions correspond to the formation-R29 and R30- and destruction-R31- of the nitrogen dioxide. The chain branching reaction R29 accounts for the majority of the NO_2 formed in the flame base. The reactions R30, and R31 are occurring between the nitrogen oxides and O radicals. Near the flame kernel when the oxidization reactions are taking place, the NO, NO_2 or other big bodies could not easily find and react with O

radicals. Indeed, highly reactive species such as H and OH do not allow O to take part in R30, and R31.

Fig 6-c demonstrates the contribution of the R25 reaction in the formation of the NO from N_2O which is terminologically known as N_2O pathway mechanism. The contribution of this mechanism is worthy of discussion for this flame in NO formation as it is important when the combustion pressure is high or the combustion temperatures is low [92]. Fig 6-c confirms despite the autoignition low temperatures, the spatial contribution of the N_2O pathway mechanism is still significantly lower than the thermal NO (see the order of magnitudes in Fig 6-a & c). The increase in coflow temperature slightly increase the rate of NO from N_2O pathway mechanism. This figure also demonstrates that the influence of temperature on NO formation from the N_2O pathway mechanism is not as much as it is in the thermal NO sub-reactions.

In summary, it should be pointed out that the dominant nitrogen oxide near the flame base is NO. Any formed NO_2 at the flame kernel from reaction R29 and R30 will be dramatically destructed by progression of the autoignition via H radicals in as it could observed in contour plot of NO_2 without any observed extensions downstream of the fuel nozzle. The majority of NO_2 correspond to the side of the fuel jet before any flame appears. The N_2O pathway mechanism is also found to have a low contribution to the level of NO.

3.2.2 Jet temperature

Similar to coflow temperature, fuel temperature may influence the formation of nitrogen oxides. Fig 7 gives the counter plots of the NO, NO_2, and N_2O for run 14, 1, 15, and 16 for which the jet temperature was at 280, 305, 340, and 360 K. This figure authenticates that the shape of fume and the level of nitrogen species is perceptibly changed during the autoignition by changing the temperature of the reactant. The increase in the jet temperature leads to less formation of NO and NO_2. It also limits the propagation of nitrogen monoxide in the turbulent flame- the NO contour contracts and the strong gradient in NO mass fraction disappears. At his condition, the simulated flame imitates the characteristics of moderate or intensive low oxygen dilution (MILD) [93].

The contribution of elementary reactions in the formation of nitrogen species is given in Fig 8. The rate of reactions is compared for jet temperatures 280 and 360 K at the flame centerline. These graphs show that the maximum rate of reactions shift toward the fuel nozzle by increasing the jet temperature. These trends are likely obtained due to the extension of the pressure-temperature regions to the areas diluted with the oxygen in MILD combustion. he more jet temperature results in comparatively lower rates of reactions R20, R21, and R32 and shifts the NO formation upstream of the jet flow. The jet temperature leads to the higher rates of nitrous oxide destruction and the conversion to NO. The rate of reactions R29, R30, and R31 also all decrease with the rise of temperature in the fuel jet. To sum, it could be concluded that high N_2/H_2 jet temperatures leads to less formation of nitrogen oxides.

3.2.3 The influence of coflow oxygen

The sensitivity of NO_X to oxygen concentrations is found weaker in comparison to the effect of the coflow temperature. Four distinct flames (runs: 5, 6, 7, and 8) with different mass fractions of oxygen- $Y_{O_2,C}$=0.12819, $Y_{O_2,C}$=0.164555, $Y_{O_2,C}$=0.20092, and $Y_{O_2,C}$=0.231-in the coflow were simulated with the purpose of understanding the influence of the oxygen content on the NO_X. In these case studies, the amount of the water in the vitiated coflow was kept constant and increase in oxygen content was balanced by decrease in nitrogen. The effect of nitrogen in the formation of nitrogen oxides seems to be stronger than that for the oxygen. Fig 9 indicates that oxygen results in the formation of less NO but more NO_2. The maximum mean NO mass fraction decreases from the value of around 4.0×10^{-5} to the value of around 2.6×10^{-5} with increasing the coflow oxygen mass fraction from the value $Y_{O_2,C}$=0.12819 to the value $Y_{O_2,C}$=0.231, respectively. It is also notable that that the strong gradient in mean NO mass fraction diminishes, and a more uniform distribution of NO is obtained with the increased oxygen content of the coflow. Although the increase in the oxygen has the potential to elevate the NO by elevating the intensity of the autoignition, increase of temperature, nitrogen dissociation, and hydroxyl radical, this analysis shows exactly the opposite and limitation of NO formation with higher oxygen content in the coflow. The contour plots in Fig 9 also depict that the

level of nitrogen dioxide and nitrous oxide increase with more oxygen. Not only the rate of formation and destruction, but also the extension of NO_2 plume is under the influence of the coflow oxygen content. In the case of nitrous oxide, a similar trend can be observed so that rate varies and reactive zone for N_2O extends. How these trends are obtained is further discussed in the analysis of rate of reactions. However, what is quite apparent is the stronger influence of coflow nitrogen compared to the oxygen in NO formation-although N_2 and O_2 both could increase the level of NO, in this case more oxygen which is balanced by less coflow nitrogen leads to reduction of NO.

Fig 10-a gives the evolution of the elementary reactions R20, R21, R22, and R32 into the formation and destruction of NO for two mass fractions 0.12819 and 0.231 of oxygen in the coflow. This figure shows that rate of NO formation from destruction of NO_2 in R32 increases and that from R22 decreases noticeably. However, the rate of R21 in the formation and R20 in destruction is not much under the influence of coflow oxygen. Fig 10-b shows the rate of reactions in the formation-R29 and R30- and destruction-R31- of nitrogen dioxide. This figure shows that the oxygen increases the rate of NO_2 destruction significantly in the axis of the flame. The oxygen also extends contour shape of nitrogen dioxide. Fig 10-c gives the spatial evolution of the R25 rate of reaction. This figure shows that oxygen raises the formation of NO from N_2O pathway mechanism. In sum, the oxygen concentrations affect the reactions rates near flame base. It could increase the rate of NO_2 destruction and conversion to NO.

To sum, the increase in jet temperature and coflow oxygen leads to lower levels of NO in autoignition, although it elevates the temperature of ignition. This is likely due to the stabilization of this flame in a more extended area, and volumetric nature of ignition compared to conventional nonpremixed and premixed flames.

3.2.4 The influence of coflow water content

The water can reduce NO_X emission in most of flames [94-97]. For this flame, the influence of water on the formation of nitrogen oxides during autoignition is analyzed here. Two simulations have been conducted: first with water replacing oxygen and second with water in the place of nitrogen.

This comparison is made in Fig 11 for runs: (a) 9, (b) 10, and (c) 11 showing the impact of water in place of oxygen. The contour plots in the Fig 11 was for $Y_{N_2,C}$=0.769 (a: $Y_{H_2O,C}$=0, $Y_{O_2,C}$=0.231, b: $Y_{H_2O,C}$=0.03228, $Y_{O_2,C}$=0.19872, c: $Y_{H_2O,C}$=0.06456, $Y_{O_2,C}$=0.16644). Fig 11 substantiates that the water decreases the NO and N_2O although it increases the NO_2. When the amount of nitrogen remains constant and coflow water content increases, the amount of oxygen in return reduces to offset the increase of water. Previously, it was observed that the NO increase by decrease in coflow oxygen. Here, a completely different trend of nitrogen oxides with the variation in oxygen is observed which shows the effective rule of water in NO_X of this flame. The decrease of NO could also be imputed to the decrease of temperature by adding water-the spatial temperature in the combustor goes down by replacing two atomic gases such as oxygen with water because three atomic gases like water have a higher specific heat C_P and require more energy than two atomic gas N_2 to show temperature increase. As a result, NO formation is limited and the formation of NO_2 would be probable. The analysis of the rates of reactions could clarify these trends. Fig 12 gives the evolution of elementary reactions participating in the nitrogen oxides. It demonstrates that the NO_2 conversion to NO increases with more coflow water. However, the rate of reaction R22 reduces remarkably. Fig 12 shows that the water also limits the formation of NO from N_2O. In the case of NO_2, the water could both increase the rate of formation (R29) and destruction of NO_2 (R31) when it replaces the oxygen.

The contour plots of nitrogen oxides mass fractions are depicted in Fig 13 when the water replaced the nitrogen. The simulations are for $Y_{O_2,C}$=0.231 (a) run 9: $Y_{H_2O,C}$=0, $Y_{N_2,C}$=0.769, (b) run 12: $Y_{H_2O,C}$ =0.03228, $Y_{N_2,C}$=0.73672 (c) run 8: $Y_{H_2O,C}$=0.06455, $Y_{N_2,C}$=0.70444 (d) run 13: $Y_{H_2O,C}$=0.12912, $Y_{N_2,C}$=0.63988. Comparing the subplots, NO and N_2O both vanish significantly with addition of water in the coflow in the replace of the nitrogen. However, the level of NO_2 increases significantly and extends widely over the entire flame plume. This is completely different from the other contours of NO_2 obtained in this study in which the NO_2 plume has a limited shape and did not evolve in the turbulent flame. Fig 14 demonstrates that the rates of R22, R32, and R25 decrease when the water

replaces the nitrogen. However, the water in the coflow could increase both the rate of formation and destruction of NO_2 in runs 9, 12, and 8 with $Y_{H_2O,C}$=0, $Y_{H_2O,C}$=0.03228, and $Y_{H_2O,C}$=0.06228, respectively. For run 13 with the most water $Y_{H_2O,C}$=0, the rate of NO_2 destruction from R31 ($NO_2 + O \rightarrow NO + O_2$) decrease and shift towards the fuel nozzle, thereby leading to the NO_2 evolution in autoignition.

The effect of water on other characteristics of this flame was previously studied. The water was confirmed to increase the lift off height of this flame [98]. Similarly, the addition of water to the coflow stream also shifts the nitrogen oxides plume further downstream. To sum, the water acts as a third body with a higher heat capacity than oxygen and nitrogen. This leads to noticeable lower combustion temperature and could explain the less formation of nitrogen oxide and nitrous oxide and more nitrogen dioxide.

3.2.5 The influence of jet nitrogen

The results of the simulation for different amount of nitrogen and hydrogen in the fuel jet are presented in the Fig 15. Fig 15 contains five sub contour plots: (a) run 17; $Y_{H_2,J}$=0.01544, $Y_{N_2,J}$ =0.98456 (b) run 18; $Y_{H_2,J}$=0.01944, $Y_{N_2,J}$=0.98056 (c) run 19; $Y_{H_2,J}$=0.04688, $Y_{N_2,J}$=0.95312 (d) run 20; $Y_{H_2,J}$=0.07032, $Y_{N_2,J}$=0.92968 (e) run 21; $Y_{H_2,J}$=0.23440, $Y_{N_2,J}$=0.7656. The simulation with different H_2/N_2 concentrations shows that the NO_X is under the strong influence of nitrogen/hydrogen content. The shapes of nitrogen oxides plume vary for different nitrogen content. The local mean mass fractions are also different from case to case. The run 21 with the highest hydrogen content has the most potential in NO formation, although the flame nitrogen is lower. The temperature in run 21 is higher (maximum temp=2140 K) than other simulation runs. The run 17 with the lowest hydrogen and highest nitrogen has the less potential for NO formation than other simulation runs. Here, the nitrogen in the jet could dilute the hydrogen well leading to the less formation of NO. This is completely opposite of what observed in contour plots Fig 5 where the nitrogen in the coflow led to more NO formation. These observations make this point clear that simultaneous control of the

hydrogen fuel and NO_X is possible with N_2 gas. According to expectations, the N_2O and NO_2 increases and decreases concomitantly with the removal of N_2 from the fuel jet, increase in H_2, and intensity of the combustion. Another significant finding of the present simulation is that the relative mean mass fractions of NO and NO_2 vary remarkably from an almost the same order of magnitudes in run 17 to levels which is significantly higher for NO compared NO_2 in run 21. In run 21, the combustion of hydrogen may change from autoignition to an ordinary diffusion flame with level of NO comparatively higher than NO_2.

The contribution of elementary reactions is to be analyzed in this paragraph to show how the addition and removal of nitrogen in the fuel jet impact the nitrogen oxides of an autoignited H_2/N_2 flame. Fig 16 demonstrates the relative contribution of elementary reactions in the formation and the destruction of NO, NO_2 and N_2O radicals near the flame base and compares the rates of elementary reactions during autoignition. The nitrogen could remarkably reduce the rate of R20-21-22 and R32. The hydrogen in the jet also elevates formation of NO from N_2O shifting the R25 reaction to the downstream of fuel nozzle. Fig 16 also shows that the contribution of the rates of reactions in the production and consumption of NO_2 lowers as the hydrogen increases in the fuel jet. The nitrogen in the hydrogen does not only harness the hydrogen flame leading to disappearance of the flame front, and sharp specie and temperature gradients, but it also limits the formation of NO, and N_2O.

In sum, this part of the manuscript shows that the NO could decrease significantly when the fuel jet is diluted with nitrogen. It could lessen the NO to a level which is the same order of magnitude with the NO_2. Whatever the condition is, N_2O level is comparatively lower than NO and NO_2 during the autoignition. Hence, NO_X during the autoignition is the mixture of nitrogen oxide and nitrogen dioxide with their level both significant and comparable.

3.2.6 Equivalence ratio

A standard parameter able to show the combined impact of the all variables is used here. The equivalence ratio can determine the state of the combustion including the final temperature, pressure, and composition of the products. For this flame, the equivalence ratio of the hot vitiated coflow is a

good choice to the study the nitrogen oxides, as it represents an overall factor including the influence of all operating points. The coflow consists of the 2000 hydrogen flame surrounding the H_2/N_2 hybrid flame. Since the flame usually lifts from the nozzle, the species in the coflow reach the chemical equilibrium before the occurrence of autoignition. Equilibrium data of hydrogen flame could be used to define the thermo-physical and chemical state of coflow. The equilibrium data of hydrogen combustion including equilibrium temperature and mass faction of hydrogen, nitrogen, water and oxygen is available in the Hanckock plot (Fig 17). This graph shows that the equilibrium temperature, i.e., adiabatic flame temperature, of the flame which is maximum at equivalence ratio 1.0. At equivalence ratio of lower (<1.0) and higher (>1.0) than 1.0, the incomplete combustion and the extra amount of oxygen gives rise to a lower equilibrium temperature. The experimental data for this graph was extracted from [99].

The nitrogen oxides in the H_2/N_2 turbulent flame is studied at four coflow equivalence ratios. The temperature and species mass fractions were extracted from Hankock chart for four equivalence ratios<1.0. Table 5 gives the conditions of the coflow collected from the Hancock plot. The averaged mass fractions of NO and NO_2 in the computational domain were graphically given Fig 18. The NO and NO_2 increases and decreases in relation to the equivalence ratio in the range of equivalence ratio [0.24 0.2475]. In this range, the temperature of the coflow also increases with equivalence ratio. The fact that both NO and temperature increase with coflow equivalence ratio means the influence of ER is similar to coflow temperature in NO_X formation during autoignition.

The strong sensitivity of the flame lift-off length to the temperature was obtained for this flame. The most similar case in table 5 (run 1) to the base case is in the second row (equivalence ratio=0.242) both with almost the coflow temperatures ($\cong 1045$ K). However, the concentration of coflow species are different. The contour plots of nitrogen oxides for run 1 and run 23 (coflow flames with the equivalence ratio=0.242) are given in Fig 19 showing that the level of nitrogen oxides is not the sole function of temperature during the autoignition, although the plume of nitrogen oxides are almost similar in these two cases. The level of NO is significantly higher in the flame when the coflow is at

equilibrium condition. This result is different from other characteristics of the autoignition such as: flame lift-off height which is under dominant influence of the coflow temperature. Given the equilibrium concentration of species of the coflow at equivalence ratio=0.242, the coflow flames form noticeable NO and NO_2. However, the NO and NO_2 formation is limited when the thermodynamic states of the coflow is far from equilibrium.

4. Conclusions

The formation of nitrogen oxides was simulated using the RANS/joint composition PDF in a turbulent lifted H_2/N_2 jet flame issuing into a hot vitiated coflow at different operating points. The summary of this research is as follow:

1) The level of NO and NO_2 is the same order of magnitude in autoignition. The main NO_2 forms in the flame lower boundaries and completely desturcts downstream of the turbulent jet. However, NO evolves in the vicinity of the nozzle and propagates in the turbulent jet.
2) At high coflow temperatures, reactions R32 ($NO_2 + H \rightarrow NO + OH$) and R22 ($N + OH \rightarrow NO + H$) are dominant and control the formation of NO during near the flame kernel. The reaction R29 ($NO + HO_2 \rightarrow NO_2 + OH$) control the NO_2 formation in the ignition kernel. Despite the case of NO and NO_2, the formation of NO from the N_2O is not that much under the influence of the coflow temperature.
3) The nitrogen oxides are influenced by the coflow oxygen content. However, its impact is conspicuously smaller than that of the coflow temperature. The oxygen decreases the rate of NO formation from R22 ($N + OH \rightarrow NO + H$) and increases the rate of NO_2 destruction from R31 ($NO_2 + O \rightarrow NO + O_2$).
4) The R22 ($N + OH \rightarrow NO + H$) and R31 ($NO_2 + O \rightarrow NO + O_2$) reactions evolve further downstream of the fuel nozzle when oxygen level is heightened in the hot coflow. Because the flame lifts when oxygen increases, the threshold of ignition and OH accumulation moves along the fuel jet, and as a result the evolution of R22 ($N + OH \rightarrow NO + H$) shows a similar behavior.

The OH accumulation also marks high temperatures which is appropriate for NO_2 destruction. The way O_2 impacts the formations nitrogen oxides imitates the conditions at the high temperature air combustion.

5) The effect of oxygen level is more significant on the reactions controlling the high temperature combustion. In sum, the rarefying the coflow flames with nitrogen could increase the level of NO, although it could lead to the harness of hydrogen flame.

6) Water acts as a third body with high heat capacity. Hence, it decreases the formation of NO with whatever the water is replaced for. The water curtails the nitrogen monoxide by decreasing the rates of NO formation through the reactions R21 ($N + O_2 \rightarrow NO + O$) and R22 ($N + OH \rightarrow NO + H$) and increasing the rate of NO destruction through the reaction R20 ($N + NO \rightarrow N_2 + O$). The water could limit the NO formation more when it replaced with nitrogen than with oxygen. In the case of NO_2, water in coflow improves the formation of nitrogen dioxides by increase in the rate of R29 ($NO + HO_2 \rightarrow NO_2 + OH$), especially it replaces the oxygen in the vitiated coflow. The addition of water results in the significant reduction in the rate of NO formation from N_2O pathway mechanism ($N_2O + O \rightarrow NO + NO$).

7) The influences of all operating points combined are investigated using equivalence ratio of vitiated coflow to show the dominant variable in NO_X. The simulations were indicative of a strong impact of NO and NO_2 to the equivalence ratio in way the temperature influences the formation of these nitrogen oxides. However, the level of NO and NO_2 is mainly controlled by the chemistry of the coflow rather than its temperature.

8) A noteworthy fact about the control of NO_X during the autoignition is keeping the coflow temperature below a certain level. As the coflow here imitates the characteristic of recirculation zone in real burners, significant attention should also be given to the temperature and chemistry of recirculated materials to control the NO_X.

In summary, the salient features of the autoignition in formation of NO_X is different from other flames. Although NO_X could be influenced by the jet temperature and composition, it is mainly determined by the characteristics of the vitiated coflow. Indeed, the post rather than pre ignition chemistry influences the formation of nitrogen oxide in turbulent flames.

Literature Cited:

[1] Bazooyar B, Darabkhani HG. Design and numerical analysis of a 3 kWe flameless microturbine combustor for hydrogen fuel. International Journal of Hydrogen Energy. 2019. https://doi.org/10.1016/j.ijhydene.2019.02.132

[2] Carcassi M, Fineschi F. Deflagrations of H 2–air and CH 4–air lean mixtures in a vented multi-compartment environment. Energy. 2005;30:1439-51.

[3] Ilbas M, Yılmaz İ, Kaplan Y. Investigations of hydrogen and hydrogen–hydrocarbon composite fuel combustion and NOx emission characteristics in a model combustor. International Journal of Hydrogen Energy. 2005;30:1139-47.

[4] Midilli A, Dincer I. Hydrogen as a renewable and sustainable solution in reducing global fossil fuel consumption. International Journal of Hydrogen Energy. 2008;33:4209-22.

[5] Choudhuri AR, Gollahalli S. Combustion characteristics of hydrogen–hydrocarbon hybrid fuels. International journal of hydrogen energy. 2000;25:451-62.

[6] Karim GA. Hydrogen as a spark ignition engine fuel. International Journal of Hydrogen Energy. 2003;28:569-77.

[7] Cho E-S, Chung SH. Improvement of flame stability and NOx reduction in hydrogen-added ultra lean premixed combustion. Journal of Mechanical Science and Technology. 2009;23:650-8.

[8] Choudhuri AR, Gollahalli SR. Combustion characteristics of hydrogen–hydrocarbon hybrid fuels. International Journal of Hydrogen Energy. 2000;25:451-62.

[9] Boushaki T, Dhué Y, Selle L, Ferret B, Poinsot T. Effects of hydrogen and steam addition on laminar burning velocity of methane–air premixed flame: Experimental and numerical analysis. International Journal of Hydrogen Energy. 2012;37:9412-22.

[10] Jamal Y, Wyszynski ML. On-board generation of hydrogen-rich gaseous fuels—a review. International Journal of Hydrogen Energy. 1994;19:557-72.

[11] Choudhuri AR, Gollahalli SR. Characteristics of hydrogen–hydrocarbon composite fuel turbulent jet flames. International Journal of Hydrogen Energy. 2003;28:445-54.

[12] Arteaga Mendez LD, Tummers MJ, van Veen EH, Roekaerts DJEM. Effect of hydrogen addition on the structure of natural-gas jet-in-hot-coflow flames. Proceedings of the Combustion Institute. 2015;35:3557-64.

[13] Emadi M, Karkow D, Salameh T, Gohil A, Ratner A. Flame structure changes resulting from hydrogen-enrichment and pressurization for low-swirl premixed methane–air flames. International Journal of Hydrogen Energy. 2012;37:10397-404.

[14] Cozzi F, Coghe A. Behavior of hydrogen-enriched non-premixed swirled natural gas flames. International Journal of Hydrogen Energy. 2006;31:669-77.

[15] Ying Y, Liu D. Detailed influences of chemical effects of hydrogen as fuel additive on methane flame. International Journal of Hydrogen Energy. 2015;40:3777-88.

[16] Ma F, Wang Y, Liu H, Li Y, Wang J, Zhao S. Experimental study on thermal efficiency and emission characteristics of a lean burn hydrogen enriched natural gas engine. International Journal of Hydrogen Energy. 2007;32:5067-75.

[17] Guiberti TF, Durox D, Scouflaire P, Schuller T. Impact of heat loss and hydrogen enrichment on the shape of confined swirling flames. Proceedings of the Combustion Institute. 2015;35:1385-92.

[18] Griebel P, Boschek E, Jansohn P. Lean blowout limits and NOx emissions of turbulent, lean premixed, hydrogen-enriched methane/air flames at high pressure. Journal of engineering for gas turbines and power. 2007;129:404-10.
[19] Afarin Y, Tabejamaat S. Effect of hydrogen on H2/CH4 flame structure of MILD combustion using the LES method. International Journal of Hydrogen Energy. 2013;38:3447-58.
[20] Al-Janabi HA-KS, Al-Baghdadi MA-RS. A prediction study of the effect of hydrogen blending on the performance and pollutants emission of a four stroke spark ignition engine. International Journal of Hydrogen Energy. 1999;24:363-75.
[21] Parente A, Galletti C, Tognotti L. Effect of the combustion model and kinetic mechanism on the MILD combustion in an industrial burner fed with hydrogen enriched fuels. International Journal of Hydrogen Energy. 2008;33:7553-64.
[22] Rørtveit GJ, Zepter K, Skreiberg Ø, Fossum M, Hustad JE. A comparison of low-NOx burners for combustion of methane and hydrogen mixtures. Proceedings of the Combustion Institute. 2002;29:1123-9.
[23] Han D, Mungal MG. Direct measurement of entrainment in reacting/nonreacting turbulent jets. Combustion and Flame. 2001;124:370-86.
[24] Le Cong T, Dagaut P. Experimental and detailed modeling study of the effect of water vapor on the kinetics of combustion of hydrogen and natural gas, impact on NO x. Energy & Fuels. 2009;23:725-34.
[25] Marek CJ, Smith TD, Kundu K. Low emission hydrogen combustors for gas turbines using lean direct injection. Proceedings of the 41st Joint Propulsion Conference, Tucson, AZ, July2005. p. 10-3.
[26] Bell JB, Day MS, Lijewski MJ. Simulation of nitrogen emissions in a premixed hydrogen flame stabilized on a low swirl burner. Proceedings of the Combustion Institute. 2013;34:1173-82.
[27] Oh J, Hwang J, Yoon Y. EINOx scaling in a non-premixed turbulent hydrogen jet with swirled coaxial air. International Journal of Hydrogen Energy. 2010;35:8715-22.
[28] Noda S, Inohae J, Saldi ZS. NOx emission characteristics of confined jet nonpremixed flames. Proceedings of the Combustion Institute. 2007;31:1625-32.
[29] Anderson DN. Emissions of oxides of nitrogen from an experimental premixed-hydrogen burner. 1976.
[30] Bazooyar B, Shariati A, Hashemabadi SH. Characterization and Reduction of NO during the Combustion of Biodiesel in a Semi-industrial Boiler. Energy & Fuels. 2015;29:6804-14.
[31] Laster WR, Sojka PE. Autoignition of H2-air-The effect of NOx addition. Journal of Propulsion and Power. 1989;5:385-90.
[32] Barlow RS, Carter CD. Raman/Rayleigh/LIF measurements of nitric oxide formation in turbulent hydrogen jet flames. Combustion and Flame. 1994;97:261-80.
[33] Zhang Y, Zhang H, Tian L, Ji P, Ma S. Temperature and emissions characteristics of a micro-mixing injection hydrogen-rich syngas flame diluted with N2. International Journal of Hydrogen Energy. 2015;40:12550-9.
[34] Drake MC, Blint RJ. Thermal NOx in stretched laminar opposed-flow diffusion flames with CO/H2/N2 fuel. Combustion and Flame. 1989;76:151-67.
[35] Skottene M, Rian KE. A study of NOx formation in hydrogen flames. International Journal of Hydrogen Energy. 2007;32:3572-85.
[36] Sahu AB, Ravikrishna RV. A detailed numerical study of NOx kinetics in low calorific value H2/CO syngas flames. International Journal of Hydrogen Energy. 2014;39:17358-70.
[37] Hashemi SA, Fattahi A, Sheikhzadeh GA, Mehrabian MA. Investigation of the effect of air turbulence intensity on NOx emission in non-premixed hydrogen and hydrogen-hydrocarbon composite fuel combustion. International Journal of Hydrogen Energy. 2011;36:10159-68.
[38] Saqr KM, Aly HS, Sies MM, Wahid MA. Effect of free stream turbulence on NOx and soot formation in turbulent diffusion CH4-air flames. International Communications in Heat and Mass Transfer. 2010;37:611-7.

[39] Feikema D, Chen R-H, Driscoll JF. Blowout of nonpremixed flames: Maximum coaxial air velocities achievable, with and without swirl. Combustion and Flame. 1991;86:347-58.
[40] Lee S-R, Park S-S, Chung S-H. Flame structure and thermal NOx formation in hydrogen diffusion flames with reduced kinetic mechanisms. KSME Journal. 1995;9:377-84.
[41] Kim HS, Arghode VK, Gupta AK. Flame characteristics of hydrogen-enriched methane–air premixed swirling flames. International Journal of Hydrogen Energy. 2009;34:1063-73.
[42] Oh J, Heo P, Yoon Y. Acoustic excitation effect on NOx reduction and flame stability in a lifted non-premixed turbulent hydrogen jet with coaxial air. International Journal of Hydrogen Energy. 2009;34:7851-61.
[43] Heo P-W, Oh J-S, Yoon Y-B. NOx Reduction by Acoustic Excitation on Coaxial Air Stream in Lifted Turbulent Hydrogen Non-Premixed Flame. Journal of the Korean Society of Combustion. 2009;14:31-8.
[44] Kim HS, Arghode VK, Linck MB, Gupta AK. Hydrogen addition effects in a confined swirl-stabilized methane-air flame. International Journal of Hydrogen Energy. 2009;34:1054-62.
[45] Moon H-J, Park Y-H, Yoon Y. NOx emission characteristics in turbulent hydrogen jet flames with coaxial air. Journal of mechanical science and technology. 2009;23:1751-9.
[46] Chen R-H. Some characteristics of NOx emission of turbulent nonpremixed hydrogen-air flames stabilized by swirl-generated flow recirculation. Combustion science and technology. 1995;110:443-60.
[47] Andrew L, Robert KEE, Robert D, James B. A model for detailed chemical kinetics in turbulent nonpremixed jet flames. 29th Aerospace Sciences Meeting: American Institute of Aeronautics and Astronautics; 1991.
[48] Han J-U, Jeong Y-S, Lee C-E. The effect of turbulence intensity on the NOx formation of hydrogen coaxial jet turbulent diffusion flames. Transactions of the Korean Society of Mechanical Engineers B. 2001;25:147-55.
[49] Smith NSA, Bilger RW, Chen JY. Twenty-Fourth Symposium on CombustionModelling of nonpremixed hydrogen jet flames using a conditional moment closure method. Symposium (International) on Combustion. 1992;24:263-9.
[50] Barlow RS, Smith NSA, Chen JY, Bilger RW. Nitric oxide formation in dilute hydrogen jet flames: isolation of the effects of radiation and turbulence-chemistry submodels. Combustion and Flame. 1999;117:4-31.
[51] Moon H-J. Analysis of flame shapes in turbulent hydrogen jet flames with coaxial air. Journal of mechanical science and technology. 2009;23:1743-50.
[52] Gao X, Duan F, Lim SC, Yip MS. NOx formation in hydrogen–methane turbulent diffusion flame under the moderate or intense low-oxygen dilution conditions. Energy. 2013;59:559-69.
[53] Yu Y, Gaofeng W, Qizhao L, Chengbiao M, Xianjun X. Flameless combustion for hydrogen containing fuels. International Journal of Hydrogen Energy. 2010;35:2694-7.
[54] Kashir B, Tabejamaat S, Jalalatian N. A numerical study on combustion characteristics of blended methane-hydrogen bluff-body stabilized swirl diffusion flames. International Journal of Hydrogen Energy. 2015;40:6243-58.
[55] Hwang C-H, Lee S, Lee C-E. The effect of turbulence intensity of ambient air flow on NOx emissions in H2/air nonpremixed jet flames. International Journal of Hydrogen Energy. 2008;33:832-41.
[56] Cabra R, Chen J-Y, Dibble R, Karpetis A, Barlow R. Lifted methane–air jet flames in a vitiated coflow. Combustion and Flame. 2005;143:491-506.
[57] Medwell PR, Kalt PA, Dally BB. Reaction zone weakening effects under hot and diluted oxidant stream conditions. Combustion Science and Technology. 2009;181:937-53.
[58] Gordon RL, Masri AR, Mastorakos E. Simultaneous Rayleigh temperature, OH-and CH 2 O-LIF imaging of methane jets in a vitiated coflow. Combustion and Flame. 2008;155:181-95.
[59] Wu Z, Masri AR, Bilger RW. An experimental investigation of the turbulence structure of a lifted H2/N2 jet flame in a vitiated co-flow. Flow, turbulence and combustion. 2006;76:61-81.

[60] Mouangue R, Obounou M, Mura A. Turbulent lifted flames of H 2/N 2 fuel issuing into a vitiated coflow investigated using Lagrangian Intermittent Modelling. International Journal of Hydrogen Energy. 2014;39:13002-13.
[61] Wang H, Luo K, Yi F, Fan J. Direct numerical simulation study of an experimental lifted H2/N2 flame. Part 2: flame stabilization. Energy & Fuels. 2012;26:4830-9.
[62] Luo K, Wang H, Yi F, Fan J. Direct numerical simulation study of an experimental lifted H2/N2 flame. Part 1: validation and flame structure. Energy & Fuels. 2012;26:6118-27.
[63] Wang Z, Zhou J, Cen K. Visualization of nonpremixed hydrogen jet flame in a vitiated coflow by DNS. Journal of Visualization. 2007;10:136-.
[64] Wang Z, Fan J, Zhou J, Cen K. Direct numerical simulation of hydrogen turbulent lifted jet flame in a vitiated coflow. Chinese Science Bulletin. 2007;52:2147-56.
[65] Patwardhan S, De S, Lakshmisha K, Raghunandan B. CMC simulations of lifted turbulent jet flame in a vitiated coflow. Proceedings of the Combustion Institute. 2009;32:1705-12.
[66] Michel J-B, Colin O, Angelberger C, Veynante D. Using the tabulated diffusion flamelet model ADF-PCM to simulate a lifted methane–air jet flame. Combustion and Flame. 2009;156:1318-31.
[67] Schefer RW, Kulatilaka WD, Patterson BD, Settersten TB. Visible emission of hydrogen flames. Combustion and flame. 2009;156:1234-41.
[68] Bazooyar B, Jomekian A, Shariati A. Analysis of the formation and interaction of nitrogen oxides in a rapeseed methyl ester nonpremixed turbulent flame. Energy & Fuels. 2017;31:8708-21.
[69] Cabra R, Myhrvold T, Chen J, Dibble R, Karpetis A, Barlow R. Simultaneous laser Raman-Rayleigh-LIF measurements and numerical modeling results of a lifted turbulent H 2/N 2 jet flame in a vitiated coflow. Proceedings of the Combustion Institute. 2002;29:1881-8.
[70] Masri A, Cao R, Pope S, Goldin G. PDF calculations of turbulent lifted flames of H~ 2/N~ 2 fuel issuing into a vitiated co-flow. Combustion Theory and Modelling. 2004;8:1-22.
[71] Barlow R, Fiechtner G, Carter C, Chen J-Y. Experiments on the scalar structure of turbulent CO/H 2/N 2 jet flames. Combustion and Flame. 2000;120:549-69.
[72] Li J, Zhao Z, Kazakov A, Dryer FL. An updated comprehensive kinetic model of hydrogen combustion. International journal of chemical kinetics. 2004;36:566-75.
[73] Mueller M, Kim T, Yetter R, Dryer F. Flow reactor studies and kinetic modeling of the H2/O2 reaction. International Journal of Chemical Kinetics. 1999;31:113-25.
[74] Cao RR, Pope SB, Masri AR. Turbulent lifted flames in a vitiated coflow investigated using joint PDF calculations. Combustion and flame. 2005;142:438-53.
[75] Hosseini SE, Bagheri G, Wahid MA. Numerical investigation of biogas flameless combustion. Energy conversion and management. 2014;81:41-50.
[76] Hosseini SE, Abdul Wahid M. Effects of burner configuration on the characteristics of biogas flameless combustion. Combustion Science and Technology. 2015;187:1240-62.
[77] Bazooyar B, Ghorbani A, Shariati A. Combustion performance and emissions of petrodiesel and biodiesels based on various vegetable oils in a semi industrial boiler. Fuel. 2011;90:3078-92.
[78] Lien F-S, Leschziner M. Assessment of turbulence-transport models including non-linear RNG eddy-viscosity formulation and second-moment closure for flow over a backward-facing step. Computers & Fluids. 1994;23:983-1004.
[79] Speziale CG, Sarkar S, Gatski TB. Modelling the pressure–strain correlation of turbulence: an invariant dynamical systems approach. Journal of Fluid Mechanics. 1991;227:245-72.
[80] Younis B, Gatski T, Speziale C. Assessment of the SSG pressure-strain model in free turbulent jets with and without swirl. Journal of fluids engineering. 1996;118:800-9.
[81] Nooren P, Wouters H, Peeters T, Roekaerts D, Maas U, Schmidt D. Monte Carlo PDF modelling of a turbulent natural-gas diffusion flame. 1997.
[82] Cheng P. Two-dimensional radiating gas flow by a moment method. AIAA journal. 1964;2:1662-4.
[83] Bazooyar B, Shariati A, Hashemabadi SH. Turbulent non-premixed combustion of rapeseed methyl ester in a free shear swirl air flow. Industrial & Engineering Chemistry Research. 2016;55:11645-63.

[84] Ilbas M. The effect of thermal radiation and radiation models on hydrogen–hydrocarbon combustion modelling. International Journal of Hydrogen Energy. 2005;30:1113-26.
[85] Garner W, Tawada K. The radiation from the hydrogen-oxygen flame. Transactions of the Faraday Society. 1930;26:36-45.
[86] Frassoldati A, Faravelli T, Ranzi E. A wide range modeling study of formation and nitrogen chemistry in hydrogen combustion. International Journal of Hydrogen Energy. 2006;31:2310-28.
[87] Pope SB. PDF methods for turbulent reactive flows. Progress in Energy and Combustion Science. 1985;11:119-92.
[88] Ayoub M, Rottier C, Carpentier S, Villermaux C, Boukhalfa AM, Honoré D. An experimental study of mild flameless combustion of methane/hydrogen mixtures. International Journal of Hydrogen Energy. 2012;37:6912-21.
[89] Jones W, Navarro-Martinez S. Large eddy simulation of autoignition with a subgrid probability density function method. Combustion and Flame. 2007;150:170-87.
[90] Savitzky A, Golay MJ. Smoothing and differentiation of data by simplified least squares procedures. Analytical chemistry. 1964;36:1627-39.
[91] Hill S, Smoot LD. Modeling of nitrogen oxides formation and destruction in combustion systems. Progress in energy and combustion science. 2000;26:417-58.
[92] Bazooyar B, Hashemabadi SH, Shariati A. NOX formation of biodiesel in utility power plant boilers; Part B. Comparison of NO between biodiesel and petrodiesel. Fuel. 2016;182:323-32.
[93] Cavaliere A, de Joannon M. Mild combustion. Progress in Energy and Combustion science. 2004;30:329-66.
[94] Psota M, Easley W, Fort T, Mellor A. Water injection effects on NOx emissions for engines utilizing diffusion flame combustion. SAE Technical Paper; 1997.
[95] Blevins LG, Roby RJ. An experimental study of NOx reduction in laminar diffusion flames by addition of high levels of steam. ASME 1995 International Gas Turbine and Aeroengine Congress and Exposition: American Society of Mechanical Engineers; 1995. p. V003T06A54-VT06A54.
[96] Dhyani V, Subramanian KA. Control of backfire and NOx emission reduction in a hydrogen fueled multi-cylinder spark ignition engine using cooled EGR and water injection strategies. International Journal of Hydrogen Energy. 2019.
[97] Taghavifar H, Anvari S, Parvishi A. Benchmarking of water injection in a hydrogen-fueled diesel engine to reduce emissions. International Journal of Hydrogen Energy. 2017;42:11962-75.
[98] Markides C, Mastorakos E. An experimental study of hydrogen autoignition in a turbulent co-flow of heated air. Proceedings of the Combustion Institute. 2005;30:883-91.
[99] Hancock RD, Bertagnolli KE, Lucht RP. Nitrogen and hydrogen CARS temperature measurements in a hydrogen/air flame using a near-adiabatic flat-flame burner. Combustion and Flame. 1997;109:323-31.

Symbols

áQñ	Ensemble averaging of variable Q
$\tilde{Q}$	Favre averaging of variable Q
Q''	Favre fluctuation of variable Q
á$A\|B$ñ	Conditional probability of event A, given the event B occurs
a	Absorption coefficient
A	surface area
b	Anisotropy tensor
D	Diameter
h	Enthalpy [J. mol^{-1}]
h_o	Heat transfer coefficient [W/m^2 K]
u	Velocity [$m.s^{-1}$]
P	Production term
S	Rate of strain
J	Molecular diffusion flux
M	Viscosity [$m^2.s^{-1}$]
Sc	Schmidt number
C	Constant
X	Mole fraction
Y	Mass fraction
Re	Reynolds number
D	Nozzle diameter [m]
R	Nozzle radius [m]
q	Radiation flux [W. m^{-2}. K^{-1}]
T	Temperature [K]
S	The net reaction rate [kmol. m^{-3} . s^{-1}]
u	velocity [$m.s^{-1}$]
Sc	Schmidt number
E	Equivalent emission
G	Incident radiation
W	Thickness of burner
N	Number of particles

Greek letters

ρ	Density [kg. m^{-3}]
ε	Dissipation rate [m^2. s^{-2}]
ε	Emissivity
η	Composition space vector
ϕ	Pressure stress term
ζ	Standardized normal random
χ	Mixture fraction
τ	Stress term
σ	Scattering coefficient
Ω	Rotation tensor
ν	Kinematic viscosity
Γ	Diffusivity coefficient
δ	Delta function

Subscripts

t	Turbulent
J	Jet
C	Coflow
i, j, k	Species indices
p	Particle
w	wall

Abbreviation

PDF	Probability density function
NO_X	Nitrogen oxides
NO	Nitrogen monoxide
NO	Nitrogen dioxide
N_2O	Nitrous oxide
RANS	Reynolds-Averaged Navier-Stokes
MC	Modified Curl
SSG	Speziale, Sarkar and Gatski
PRESTO	PREssure Staggering Option
PISO	Pressure Implicit with Split Operator
JHC	Jet in Hot Coflow

EDC	Eddy Dissipation Concept
CMC	Conditional moment cloture
ISAT	In Situ Adaptive Tabulation
JPDF	Joint Composition Probability Density Function
ER	Equivalence Ratio
UHC	Unburned hydrocarbons
CO_2	Carbon dioxide
CO	Carbon monoxide
MILD	Intensive Low Oxygen Dilution

Table 1 $N_2/H_2/O_2$ combustion mechanism, $k = AT^n \exp(-E/RT)$ [68].

NO	Reaction		A (cm, mol, s)	n	E (kcal mol^{-1})
(R1)	$H + O_2 \rightarrow O + OH$		3.55×10^{15}	-0.41	16.6
(R2)	$O + H_2 \rightarrow OH + H$		5.08×10^{04}	2.67	6.29
(R3)	$H_2 + OH \rightarrow H_2O + H$		2.16×10^{08}	1.51	3.43
(R4)	$O + H_2O \rightarrow OH + OH$		2.97×10^{06}	2.02	13.4
(R5)	$H_2 + M \rightarrow H + H + M$		4.58×10^{19}	-1.40	104.38
(R6)	$O + O + M \rightarrow O_2 + M^a$		6.16×10^{15}	-0.500	0.00
(R7)	$O + H + M \rightarrow OH + M^a$		4.71×10^{18}	-1.00	0.00
(R8)	$H + OH + M \rightarrow H_2O + M^a$		3.80×10^{22}	-2.00	0.00
(R9)	$H + O_2 + M \rightarrow HO_2 + M^b$	k_0	6.37×10^{20}	-1.72	0.52
		k_∞	1.48×10^{12}	0.60	0.00
(R10)	$HO_2 + H \rightarrow H_2 + O_2$		1.66×10^{13}	0.00	0.82
(R11)	$HO_2 + H \rightarrow OH + OH$		7.08×10^{13}	0.00	0.30
(R12)	$HO_2 + O \rightarrow OH + O_2$		3.25×10^{13}	0.00	0.00
(R13)	$HO_2 + OH \rightarrow H_2O + O_2$		2.89×10^{13}	0.00	-0.50
(R14)	$HO_2 + HO_2 \rightarrow H_2O_2 + O_2^c$		4.20×10^{14}	0.00	11.98
	$HO_2 + HO_2 \rightarrow H_2O_2 + O_2$		1.30×10^{11}	0.00	-1.63

(R15)	$H_2O_2 + M \rightarrow 2OH + M^d$	k_0	1.20×10^{17}	0.00	45.5
		k_∞	2.95×10^{14}	0.00	48.4
(R16)	$H_2O_2 + H \rightarrow H_2O + OH$		2.41×10^{13}	0.00	3.97
(R17)	$H_2O_2 + H \rightarrow HO_2 + H_2$		4.82×10^{13}	0.00	7.95
(R18)	$H_2O_2 + O \rightarrow OH + HO_2$		9.55×10^{06}	2.00	3.97
(R19)	$H_2O_2 + OH \rightarrow HO_2 + H_2O^c$		1.00×10^{12}	0.00	0.00
	$H_2O_2 + OH \rightarrow HO_2 + H_2O$		5.80×10^{14}	0.00	9.56
(R20)	$N + NO \rightarrow N_2 + O$		3.50×10^{13}	0.00	0.33
(R21)	$N + O_2 \rightarrow NO + O$		2.65×10^{12}	0.00	6.40
(R22)	$N + OH \rightarrow NO + H$		7.333×10^{13}	0.00	1.12
(R23)	$NO + NO \rightarrow N_2 + O_2$		3.00×10^{11}	0.00	65.0
(R24)	$N_2O + O \rightarrow N_2 + O_2$		1.40×10^{12}	0.00	10.810
(R25)	$N_2O + O \rightarrow NO + NO$		2.90×10^{13}	0.00	23.15
(R26)	$N_2O + H \rightarrow N_2 + OH$		4.40×10^{14}	0.00	18.88
(R27)	$N_2O + OH \rightarrow N_2 + HO_2$		2.00×10^{12}	0.00	21.06
(R28)	$N_2O + M \rightarrow N_2 + O + M$		1.30×10^{11}	0.00	59.62
(R29)	$NO + HO_2 \rightarrow NO_2 + OH$		2.11×10^{12}	0.00	-0.48
(R30)	$NO + O + M \rightarrow NO_2 + M$		1.06×10^{20}	-1.41	0.00

(R31)	$NO_2 + O \rightarrow NO + O_2$	3.90×10^{12}	0.00	-0.24
(R32)	$NO_2 + H \rightarrow NO + OH$	1.32×10^{14}	0.00	0.360

[a] Efficiency factor for $\varepsilon_{H_2O} = 12$ and $\varepsilon_{H_2} = 12$.

[b] Troe parameter is F_c=0.8. Efficiency factor for $\varepsilon_{H_2O} = 12$. Efficiency factor for $\varepsilon_{H_2O} = 11$, $\varepsilon_{H_2} = 2$ and $\varepsilon_{O_2} = 0.78$.

[c] (R14) and (R19) are expressed as the sum of the two rate expressions.

[d] Troe parameter is F_c=0.5. Efficiency factor for $\varepsilon_{H_2O} = 12$ and $\varepsilon_{H_2} = 2.5$.

Table 2 Constants of the turbulence model

$C_1 = 3.4$, C_1^*=1.8, C_2=4.2, C_3=0.8, C_3^*=1.3, C_4=1.25, C_5=0.4, $C_{\varepsilon1}$=1.44, $C_{\varepsilon2}$=1.83, C_μ=0.09, σ_k=1.0, σ_ε=1.0

Table 3 The boundary conditions in the computational domain

Boundary condition			
Stream names	Type	Velocity	Specification method
Jet	velocity_inlet	107	5% turbulent intensity and 4.57 mm hydraulic diameter
Coflow	velocity_inlet	3.5	5% turbulent intensity and 4.57 mm turbulent lengthscale
Outlet	pressure_outlet	not defined	1 m^2/s^2 backflow turbulent kinetic energy and 1 m^2/s^3 dissipation rate

Boundary name	Type	Heat transfer
Top	Wall	$Q_{loss} = h_0 \sum A_i (T_{w,i} - T_o) + \varepsilon s \sum A_i (T_{w,i}^4 - T_0^4)$, ($h_o$=10 W/$m^2$. K, T_o=298 K, ε=0.85 s = 5.6703´ 10^{-8} 10 W/m^2. K^4)

Table 4 Operating conditions of the pressure jet type oil burner

No.	Fuel jet				Coflow				
	u (m/s)	T (K)	Y_{H_2}	Y_{N_2}	u (m/s)	T (K)	Y_{O_2}	Y_{H_2O}	Y_{N_2}
1[a]	107	305	0.02344	0.97656	3.5	1045	0.17092	0.06456	0.76452
2						1030			
3						1060			
4						1080			
5							0.12819	0.06456	0.80725
6							0.164555	0.06456	0.770885
7							0.20092	0.06456	0.73452
8							0.231	0.06456	0.70444
9							0.231	0	0.769
10							0.19872	0.03228	0.769
11							0.16644	0.06456	0.769
12							0.231	0.03228	0.73672
13							0.231	0.12912	0.63988
14		280							
15		340							

16	360		
17		0.01544	
18		0.01944	
19		0.04688	
20		0.07032	
21		0.23440	

All compositions are mass fractions.
[a] Base case: the coflow temperature in the experiment is 1045 K.

Table 5 Coflow conditions at numerical experiments for analysis of ER

ER.					No.
	T(K)	Y_{O_2}	Y_{H_2O}	Y_{N_2}	
0.24	1038.812	0.175752	0.06250335	0.7616943	22
0.242	1044.106	0.1752778	0.06302053	0.7616487	23
0.245	1052.028	0.1745665	0.06379618	0.7615803	24
0.2485	1061.239	0.1737367	0.06470094	0.7615003	25

All compositions are mass fractions.

LIST OF FIGURES

Fig 11 ..... The influence of coflow water on the formation of nitrogen oxides when water replace oxygen with $Y_{N_2,C}$=0.769 (**a: run 9;** $Y_{H_2O,C}$=0, $Y_{O_2,C}$=0.231, **b: run 10;** $Y_{H_2O,C}$ =0.03228, $Y_{O_2,C}$=0.19872, **c: run 11;** $Y_{H_2O,C}$=0.06456, $Y_{O_2,C}$=0.16644).

Fig 12 ..... The contribution of thermal NO elementary reactions to the production and consumption of nitrogen monoxide near the flame kernel along the axis of the burner when water replaces oxygen: **run 9 (dash dot line);** $Y_{H_2O,C}$=0, **run 10 (dashed line);** $Y_{H_2O,C}$=0.03228, **run 11 (solid line)**; $Y_{H_2O,C}$=0.06455 in Table 4.

Fig 13 ..... The influence of coflow water on the formation of nitrogen oxides when water replace nitrogen with $Y_{O_2,C}$=0.231 (**a: run 9;** $Y_{H_2O,C}$=0 $Y_{N_2,C}$=0.769, **b: run 12;** $Y_{H_2O,C}$ =0.03228 $Y_{N_2,C}$=0.73672, **c: run 8;** $Y_{H_2O,C}$=0.06456 $Y_{N_2,C}$=0.70444, **d: run 13;** $Y_{H_2O,C}$=0.12912 $Y_{N_2,C}$=0.63988).

Fig 14 ..... The contribution of thermal NO elementary reactions to the production and consumption of nitrogen monoxide near the flame kernel along the axis of the burner when water replaces nitrogen with $Y_{O_2,C}$=0.231: **run 9 (dash dot-dot line);** $Y_{H_2O,C}$=0, **run 12 (dash dot line);** $Y_{H_2O,C}$=0.03228, **run 8 (dashed line);** $Y_{H_2O,C}$=0.06455, **run 13 (solid line);** $Y_{H_2O,C}$=0.12912 in Table 4.

Fig 15 ..... The influence of jet nitrogen content on the formation of nitrogen oxides (**run 17;** $Y_{H_2,J}$=0.01544 $Y_{N_2,J}$=0.98456, **run 18;** $Y_{H_2,J}$=0.01944 $Y_{N_2,J}$=0.98056, **run 19;** $Y_{H_2,J}$ =0.04688 $Y_{N_2,J}$=0.95312, **run 20;** $Y_{H_2,J}$=0.07032 $Y_{N_2,J}$=0.92968, **run 21;** $Y_{H_2,J}$=0.2344 $Y_{N_2,J}$ =0.76560 in Table 4).

Fig 16 ..... The contribution of thermal NO elementary reactions

to the production and consumption of nitrogen monoxide near the flame kernel along the axis of the burner: **run 17 (long dash line)**; $Y_{H_2,J}$=0.01544 $Y_{N_2,J}$=0.98456, **run 18 (dash dot-dot line)**; $Y_{H_2,J}$=0.01944 $Y_{N_2,J}$=0.98056, **run 19 (dash dot line)**; $Y_{H_2,J}$=0.04688 $Y_{N_2,J}$=0.95312, **run 20 (dashed line)**; $Y_{H_2,J}$=0.07032 $Y_{N_2,J}$=0.92968, **run 21(solid line);** $Y_{H_2,J}$=0.2344 $Y_{N_2,J}$=0.76560 in Table 4.

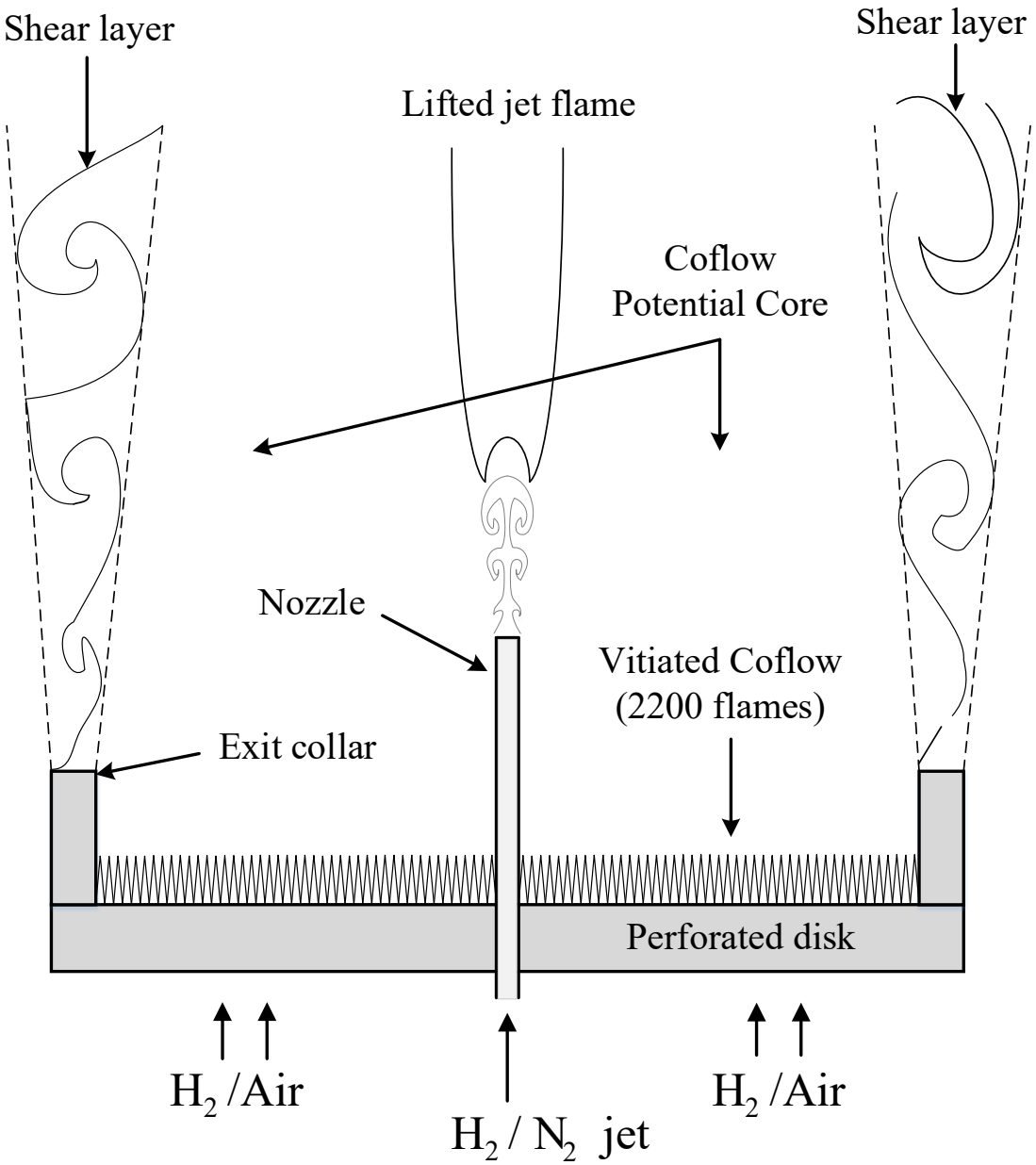
Shear layer
Shear layer
Lifted jet flame
Coflow
Potential Core
Nozzle
Vitiated Coflow
(2200 flames)
Exit collar
Perforated disk
H2 /Air
H2 / N2 jet
H2 /Air

Fig 1

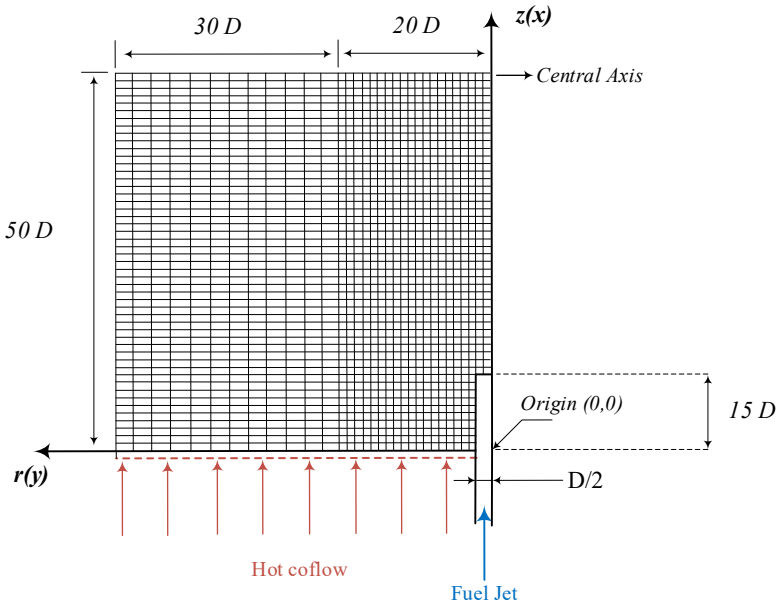
30 D
20 D
z(x)
Central Axis
50 D
Origin (0,0)
15 D
r(y)
D/2
Hot coflow
Fuel Jet

Fig 2

e

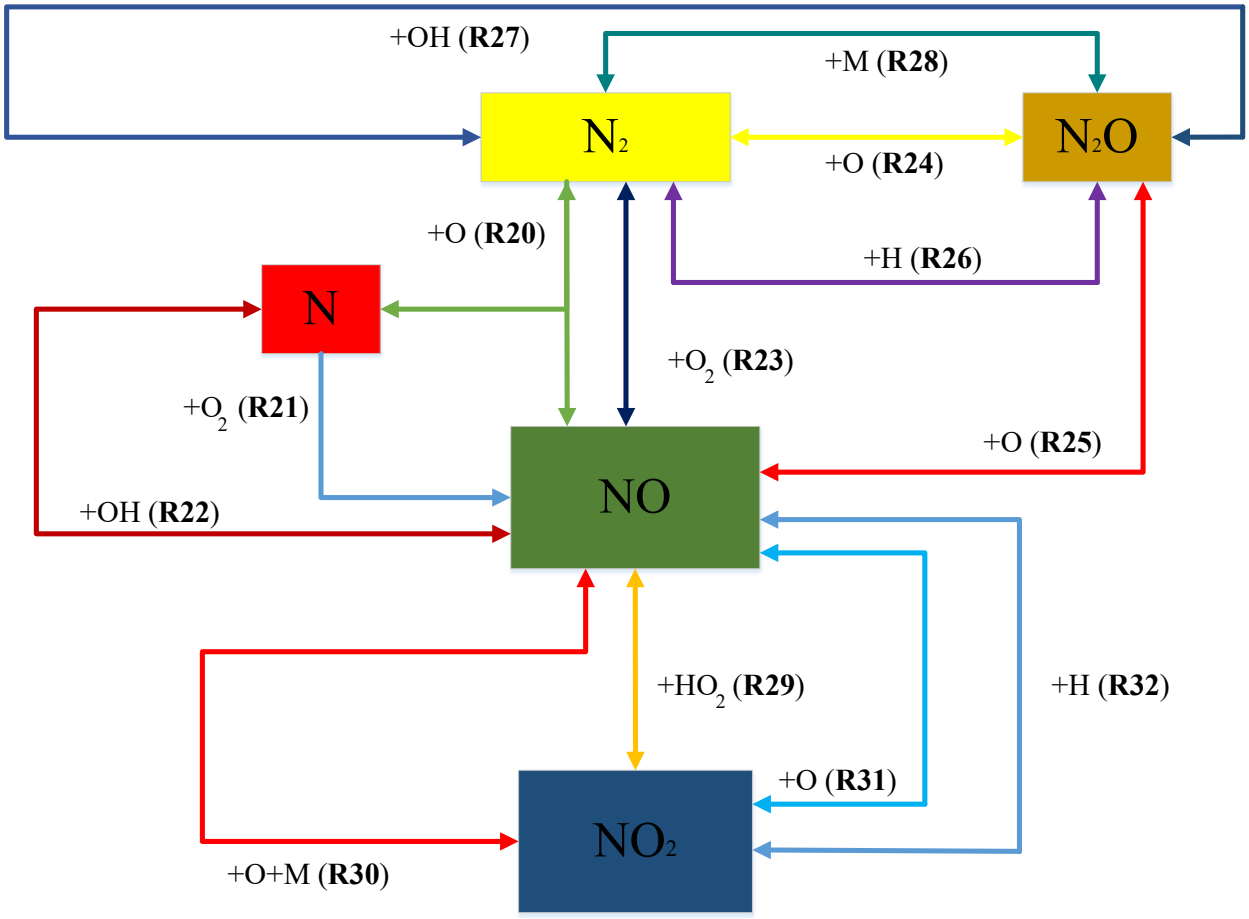
+OH (R27)
+M (R28)
N2
N2O
+O (R24)
+O (R20)
+H (R26)
N
+O2 (R23)
+O2 (R21)
+O (R25)
NO
+OH (R22)
+HO2 (R29)
+H (R32)
+O (R31)
NO2
+O+M (R30)

Fig 3

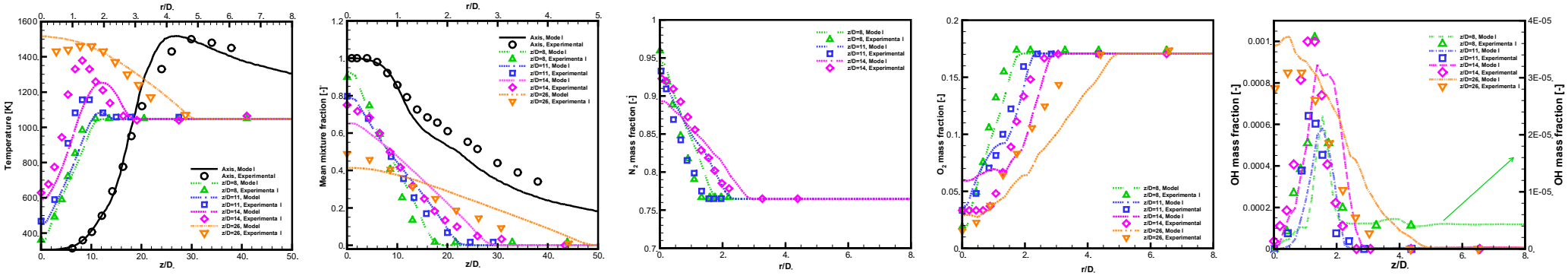
r/D.
Temperature [K]
z/D.
Axis, Mode l
Axis, Experimental
z/D=8, Mode l
z/D=8, Experimenta l
z/D=11, Mode l
z/D=11, Experimental
z/D=14, Mode l
z/D=14, Experimental
z/D=26, Mode l
z/D=26, Experimenta l
Mean mixture fraction [-]
N2 mass fraction [-]
O2 mass fraction [-]
OH mass fraction [-]

Fig 4

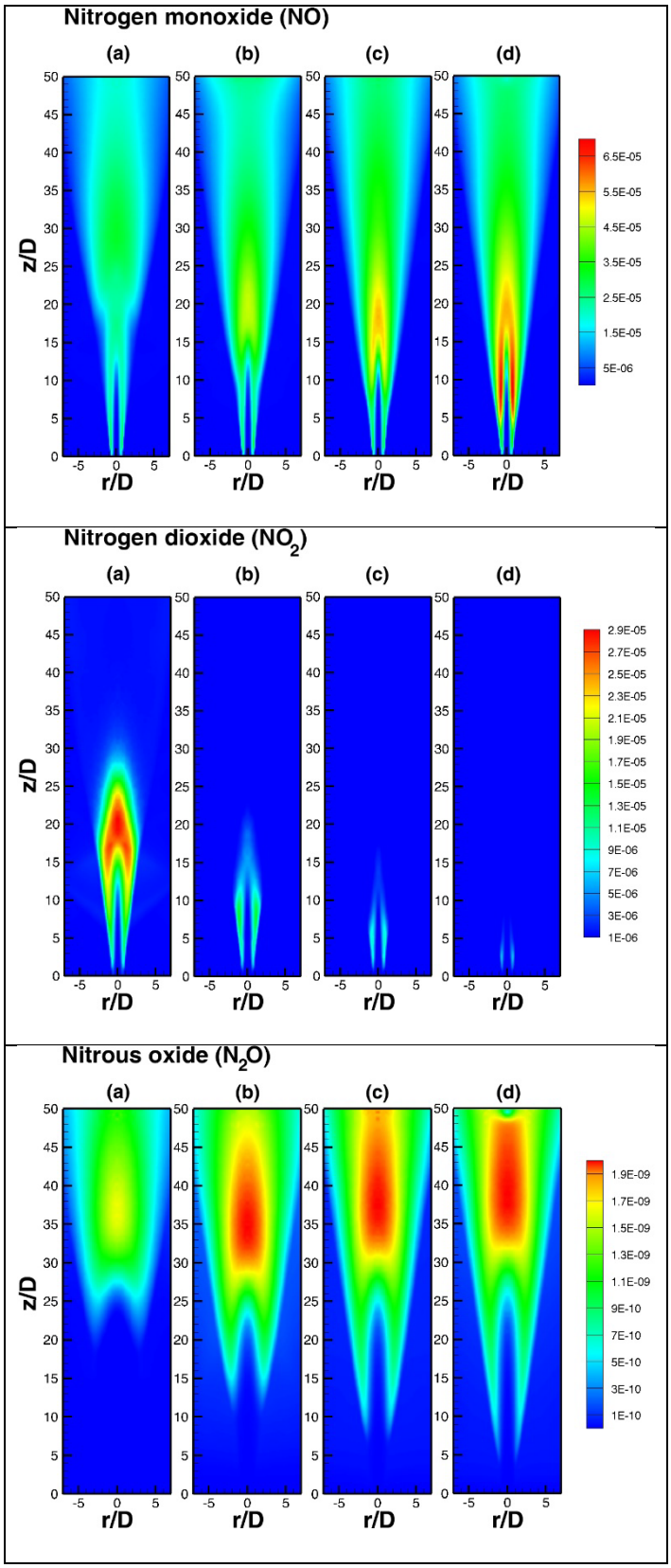
Nitrogen monoxide (NO)
(a)
(b)
(c)
(d)
z/D
r/D
6.5E-05
5.5E-05
4.5E-05
3.5E-05
2.5E-05
1.5E-05
5E-06
Nitrogen dioxide (NO2)
2.9E-05
2.7E-05
2.5E-05
2.3E-05
2.1E-05
1.9E-05
1.7E-05
1.5E-05
1.3E-05
1.1E-05
9E-06
7E-06
5E-06
3E-06
1E-06
Nitrous oxide (N2O)
1.9E-09
1.7E-09
1.5E-09
1.3E-09
1.1E-09
9E-10
7E-10
5E-10
3E-10
1E-10

Fig 5

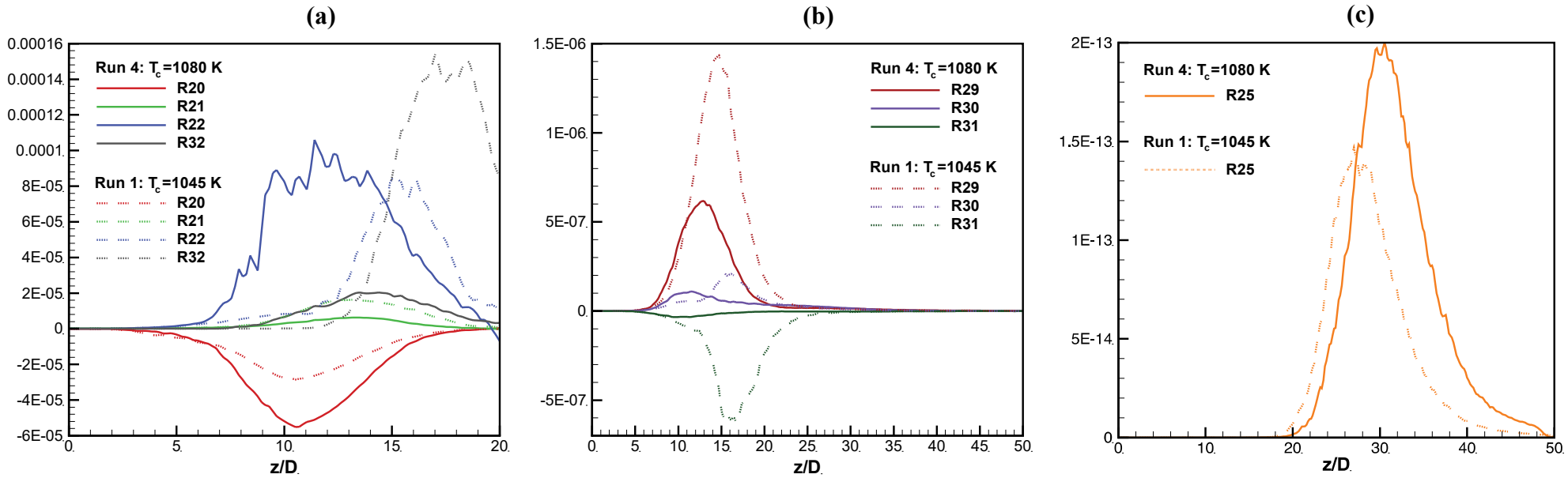
(a)
Run 4: T_c=1080 K
R20
R21
R22
R32
Run 1: T_c=1045 K
R20
R21
R22
R32
z/D
(b)
Run 4: T_c=1080 K
R29
R30
R31
Run 1: T_c=1045 K
R29
R30
R31
z/D
(c)
Run 4: T_c=1080 K
R25
Run 1: T_c=1045 K
R25
z/D

Fig 6

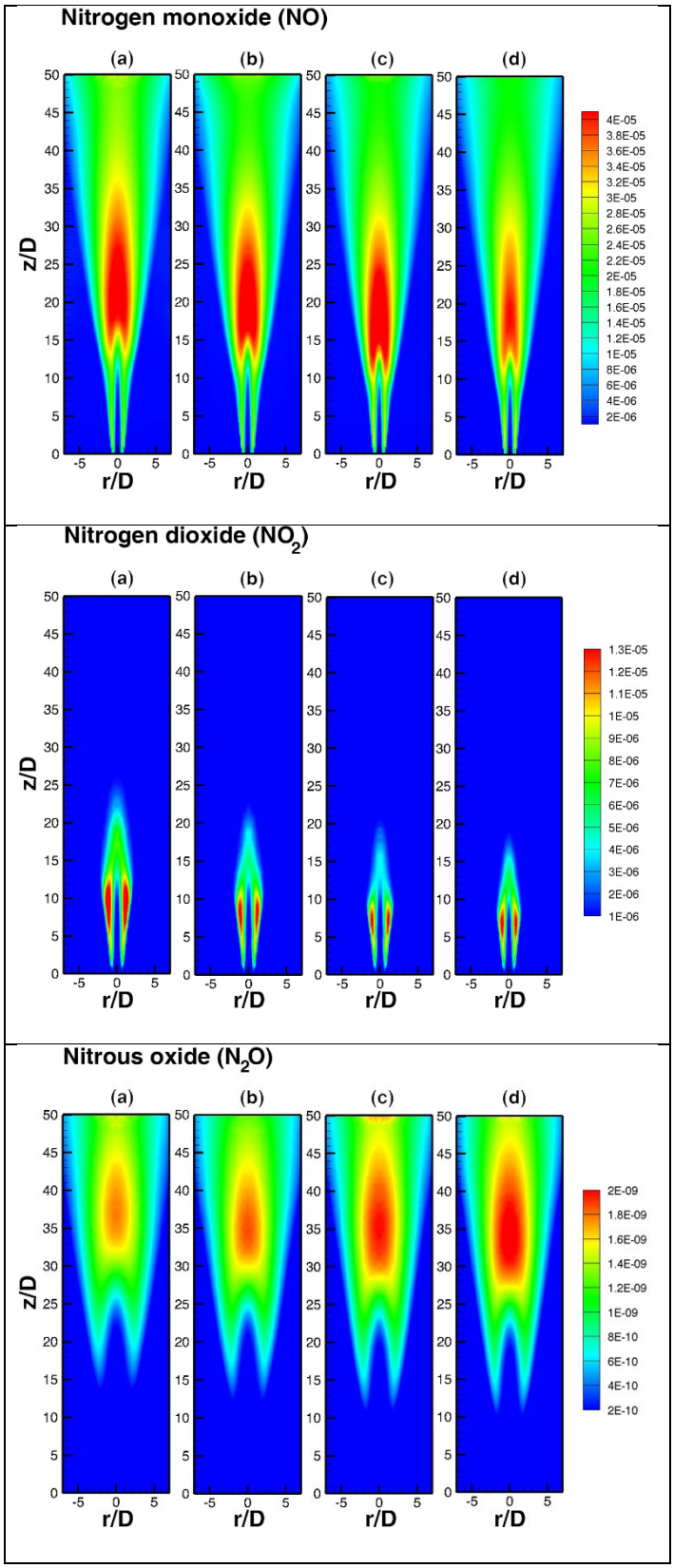
Nitrogen monoxide (NO)
(a)
(b)
(c)
(d)
z/D
r/D
4E-05
3.8E-05
3.6E-05
3.4E-05
3.2E-05
3E-05
2.8E-05
2.6E-05
2.4E-05
2.2E-05
2E-05
1.8E-05
1.6E-05
1.4E-05
1.2E-05
1E-05
8E-06
6E-06
4E-06
2E-06
Nitrogen dioxide (NO2)
1.3E-05
1.2E-05
1.1E-05
1E-05
9E-06
8E-06
7E-06
6E-06
5E-06
4E-06
3E-06
2E-06
1E-06
Nitrous oxide (N2O)
2E-09
1.8E-09
1.6E-09
1.4E-09
1.2E-09
1E-09
8E-10
6E-10
4E-10
2E-10

Fig 7

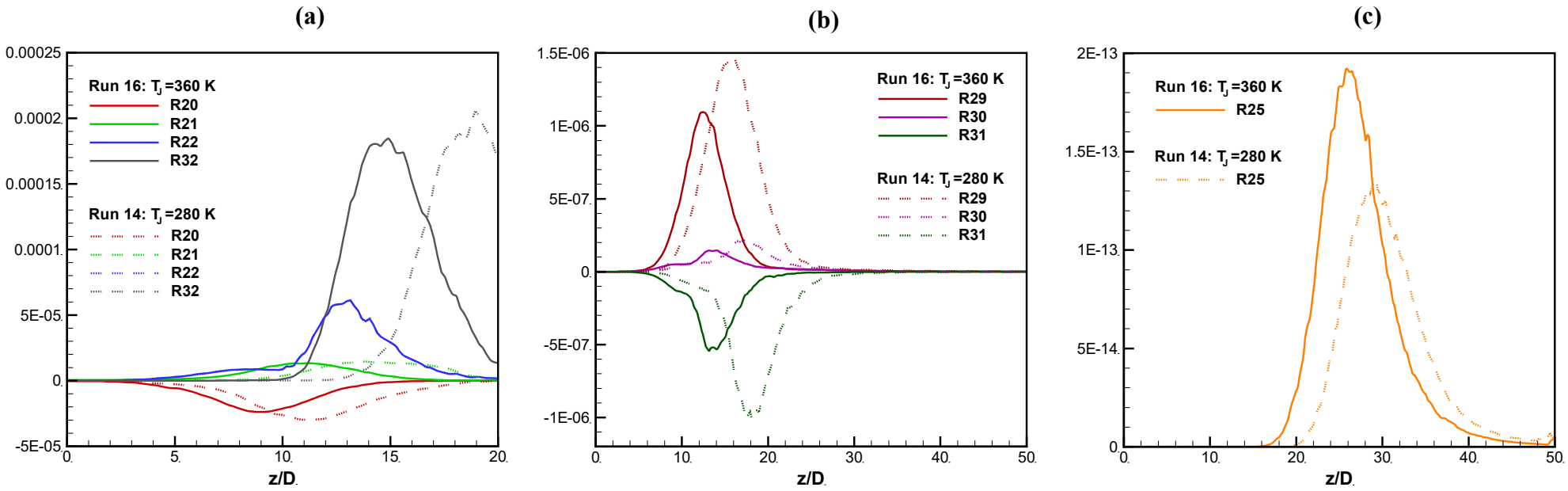
(a)
0.00025
0.0002
0.00015
0.0001
5E-05
0
-5E-05
Run 16: T_J =360 K
R20
R21
R22
R32
Run 14: T_J =280 K
R20
R21
R22
R32
0
5
10
15
20
z/D
(b)
1.5E-06
1E-06
5E-07
0
-5E-07
-1E-06
Run 16: T_J =360 K
R29
R30
R31
Run 14: T_J =280 K
R29
R30
R31
0
10
20
30
40
50
z/D
(c)
2E-13
1.5E-13
1E-13
5E-14
0
Run 16: T_J =360 K
R25
Run 14: T_J =280 K
R25
0
10
20
30
40
50
z/D

Fig 8

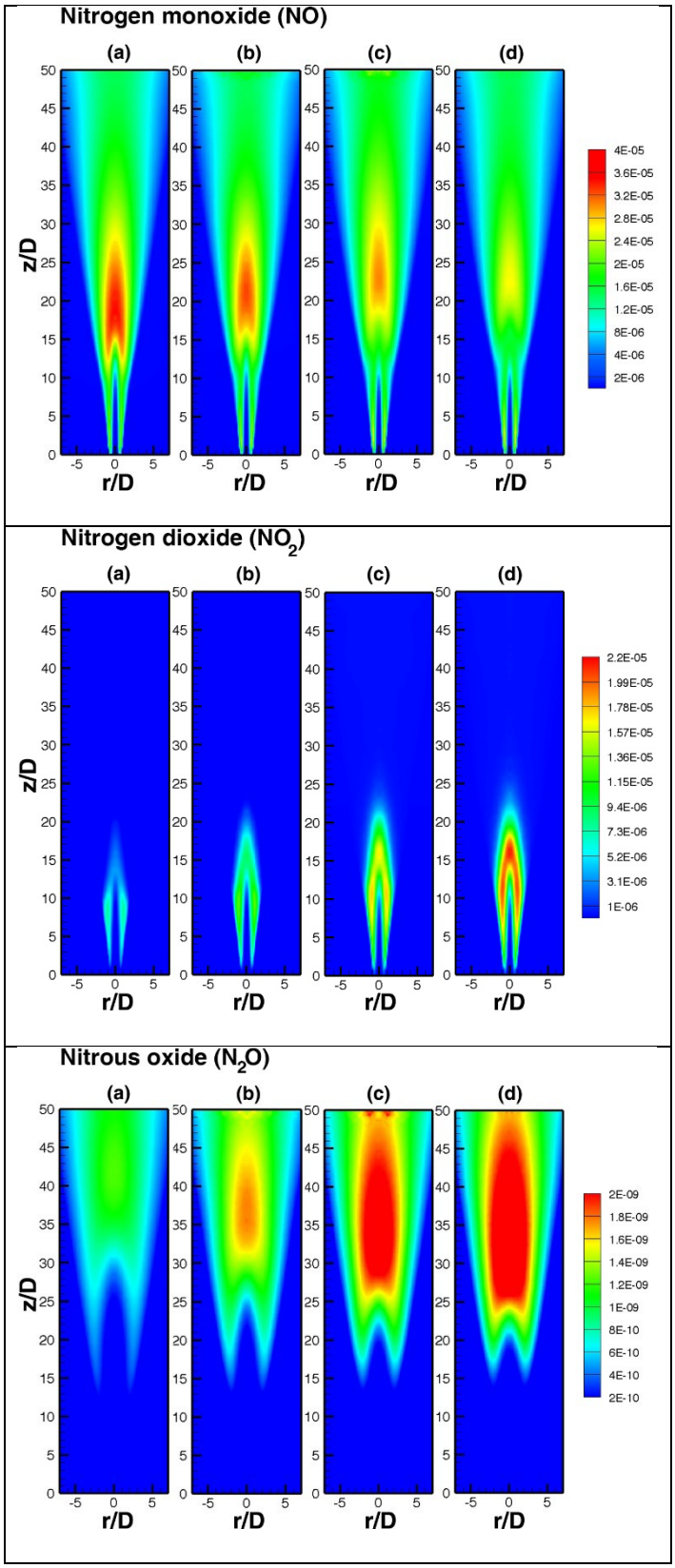
Nitrogen monoxide (NO)
(a)
(b)
(c)
(d)
z/D
r/D
4E-05
3.6E-05
3.2E-05
2.8E-05
2.4E-05
2E-05
1.6E-05
1.2E-05
8E-06
4E-06
2E-06
Nitrogen dioxide (NO2)
2.2E-05
1.99E-05
1.78E-05
1.57E-05
1.36E-05
1.15E-05
9.4E-06
7.3E-06
5.2E-06
3.1E-06
1E-06
Nitrous oxide (N2O)
2E-09
1.8E-09
1.6E-09
1.4E-09
1.2E-09
1E-09
8E-10
6E-10
4E-10
2E-10

Fig 9

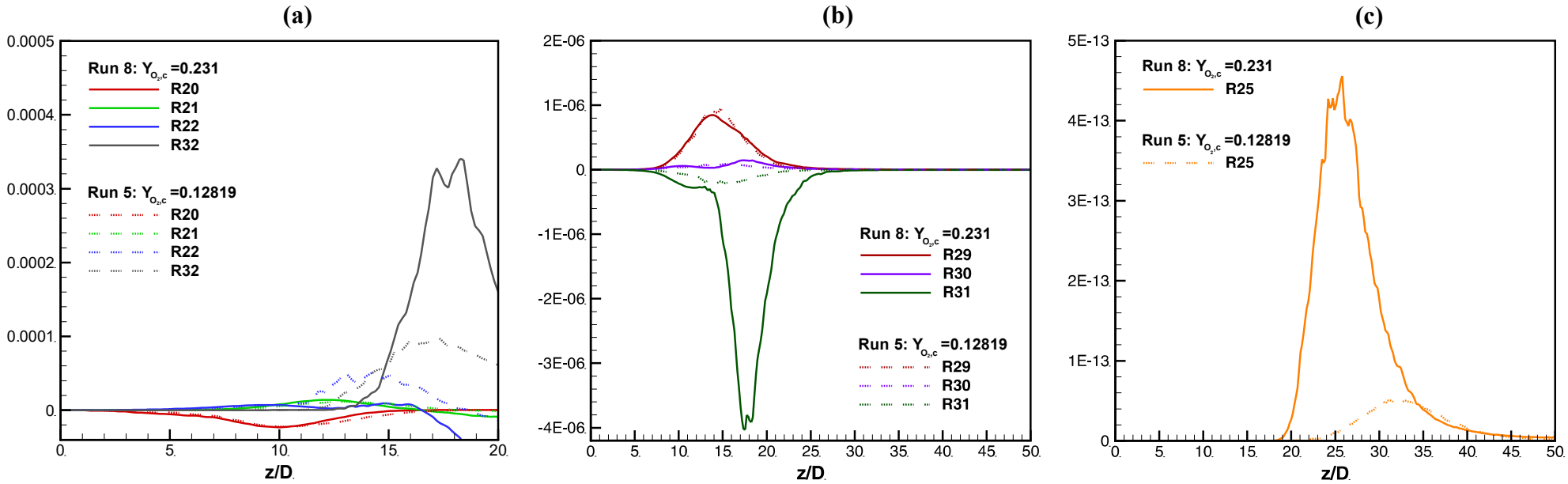
(a)
Run 8: $Y_{O_2,c}$ =0.231
R20
R21
R22
R32
Run 5: $Y_{O_2,c}$ =0.12819
R20
R21
R22
R32
0.0005
0.0004
0.0003
0.0002
0.0001
0
0
5
10
15
20
z/D
(b)
Run 8: $Y_{O_2,c}$ =0.231
R29
R30
R31
Run 5: $Y_{O_2,c}$ =0.12819
R29
R30
R31
2E-06
1E-06
0
-1E-06
-2E-06
-3E-06
-4E-06
0
5
10
15
20
25
30
35
40
45
50
z/D
(c)
Run 8: $Y_{O_2,c}$ =0.231
R25
Run 5: $Y_{O_2,c}$ =0.12819
R25
5E-13
4E-13
3E-13
2E-13
1E-13
0
0
5
10
15
20
25
30
35
40
45
50
z/D

Fig 10

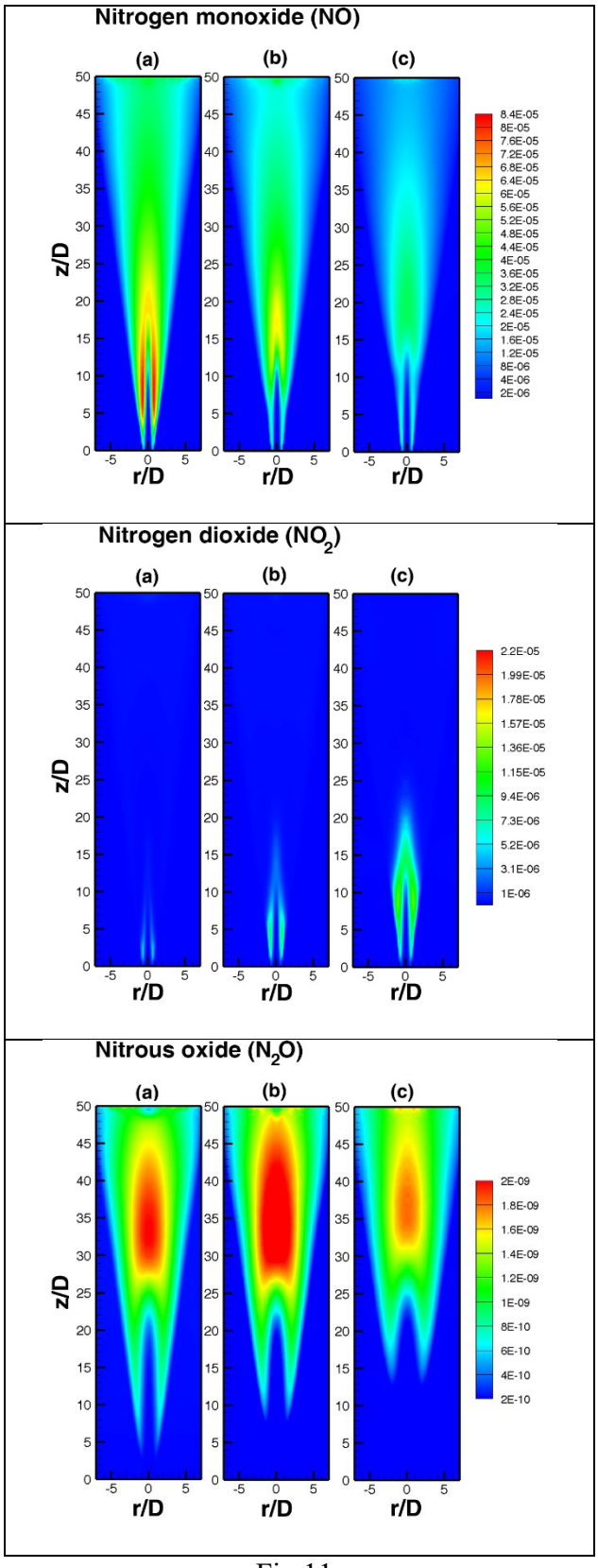
Nitrogen monoxide (NO)
(a)
(b)
(c)
z/D
r/D
8.4E-05
8E-05
7.6E-05
7.2E-05
6.8E-05
6.4E-05
6E-05
5.6E-05
5.2E-05
4.8E-05
4.4E-05
4E-05
3.6E-05
3.2E-05
2.8E-05
2.4E-05
2E-05
1.6E-05
1.2E-05
8E-06
4E-06
2E-06
Nitrogen dioxide (NO2)
2.2E-05
1.99E-05
1.78E-05
1.57E-05
1.36E-05
1.15E-05
9.4E-06
7.3E-06
5.2E-06
3.1E-06
1E-06
Nitrous oxide (N2O)
2E-09
1.8E-09
1.6E-09
1.4E-09
1.2E-09
1E-09
8E-10
6E-10
4E-10
2E-10

Fig 11

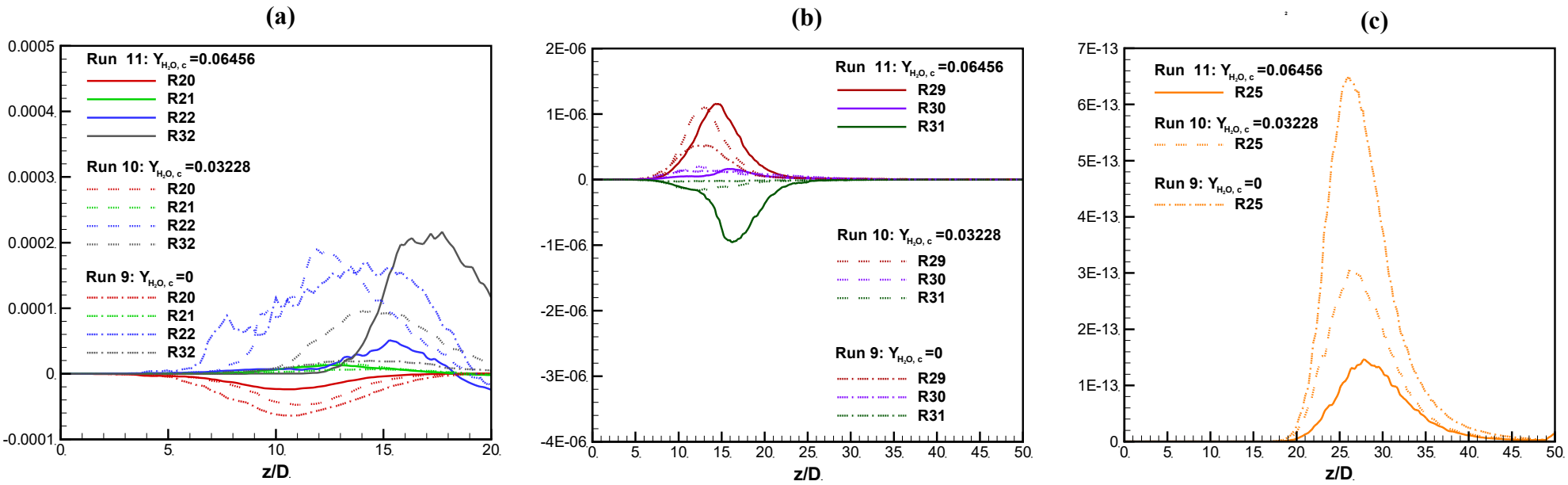
(a)
Run 11: $Y_{H_2O,c}$ =0.06456
R20
R21
R22
R32
Run 10: $Y_{H_2O,c}$ =0.03228
R20
R21
R22
R32
Run 9: $Y_{H_2O,c}$ =0
R20
R21
R22
R32
0.0005
0.0004
0.0003
0.0002
0.0001
0
-0.0001
0
5
10
15
20
z/D
(b)
Run 11: $Y_{H_2O,c}$ =0.06456
R29
R30
R31
Run 10: $Y_{H_2O,c}$ =0.03228
R29
R30
R31
Run 9: $Y_{H_2O,c}$ =0
R29
R30
R31
2E-06
1E-06
0
-1E-06
-2E-06
-3E-06
-4E-06
0
5
10
15
20
25
30
35
40
45
50
z/D
(c)
Run 11: $Y_{H_2O,c}$ =0.06456
R25
Run 10: $Y_{H_2O,c}$ =0.03228
R25
Run 9: $Y_{H_2O,c}$ =0
R25
7E-13
6E-13
5E-13
4E-13
3E-13
2E-13
1E-13
0
0
5
10
15
20
25
30
35
40
45
50
z/D

Fig 12

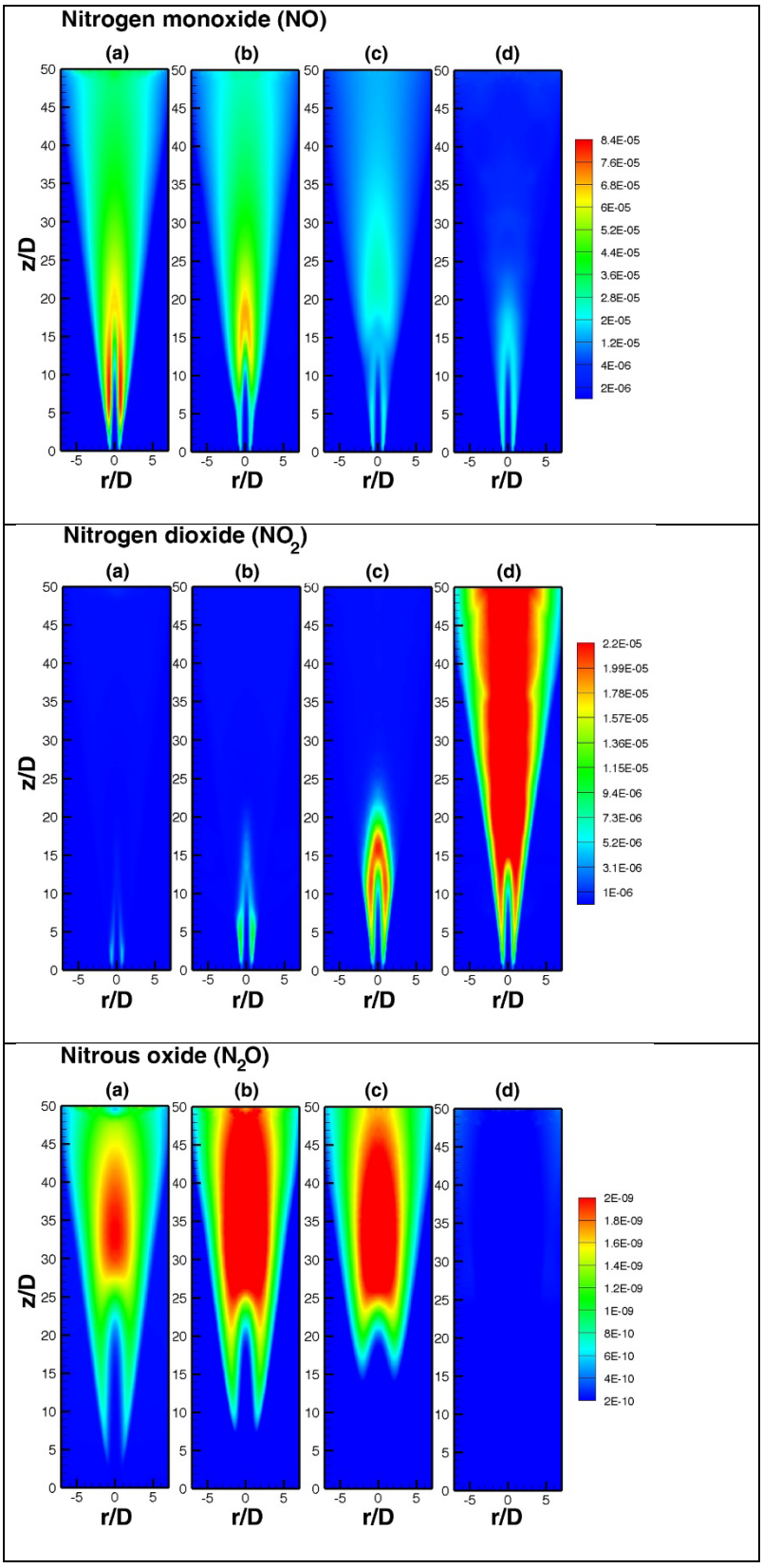
Nitrogen monoxide (NO)
(a)
(b)
(c)
(d)
z/D
r/D
8.4E-05
7.6E-05
6.8E-05
6E-05
5.2E-05
4.4E-05
3.6E-05
2.8E-05
2E-05
1.2E-05
4E-06
2E-06
Nitrogen dioxide (NO2)
2.2E-05
1.99E-05
1.78E-05
1.57E-05
1.36E-05
1.15E-05
9.4E-06
7.3E-06
5.2E-06
3.1E-06
1E-06
Nitrous oxide (N2O)
2E-09
1.8E-09
1.6E-09
1.4E-09
1.2E-09
1E-09
8E-10
6E-10
4E-10
2E-10

Fig 13

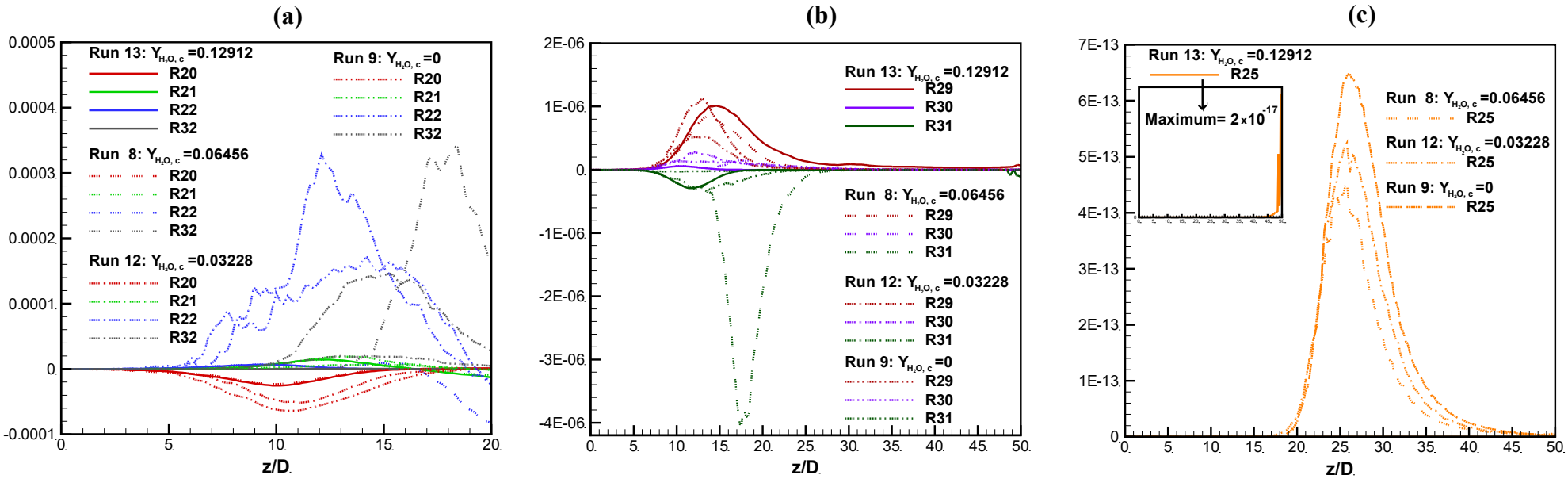
(a)
Run 13: $Y_{H_2O,c}$ =0.12912
R20
R21
R22
R32
Run 9: $Y_{H_2O,c}$ =0
R20
R21
R22
R32
Run 8: $Y_{H_2O,c}$ =0.06456
R20
R21
R22
R32
Run 12: $Y_{H_2O,c}$ =0.03228
R20
R21
R22
R32
0.0005
0.0004
0.0003
0.0002
0.0001
0
-0.0001
0.
5.
10.
15.
20.
z/D
(b)
Run 13: $Y_{H_2O,c}$ =0.12912
R29
R30
R31
Run 8: $Y_{H_2O,c}$ =0.06456
R29
R30
R31
Run 12: $Y_{H_2O,c}$ =0.03228
R29
R30
R31
Run 9: $Y_{H_2O,c}$ =0
R29
R30
R31
2E-06
1E-06
0
-1E-06
-2E-06
-3E-06
-4E-06
0.
5.
10.
15.
20.
25.
30.
35.
40.
45.
50.
z/D
(c)
Run 13: $Y_{H_2O,c}$ =0.12912
R25
Maximum= 2×10^{-17}
Run 8: $Y_{H_2O,c}$ =0.06456
R25
Run 12: $Y_{H_2O,c}$ =0.03228
R25
Run 9: $Y_{H_2O,c}$ =0
R25
7E-13
6E-13
5E-13
4E-13
3E-13
2E-13
1E-13
0
0.
5.
10.
15.
20.
25.
30.
35.
40.
45.
50.
z/D

Fig 14

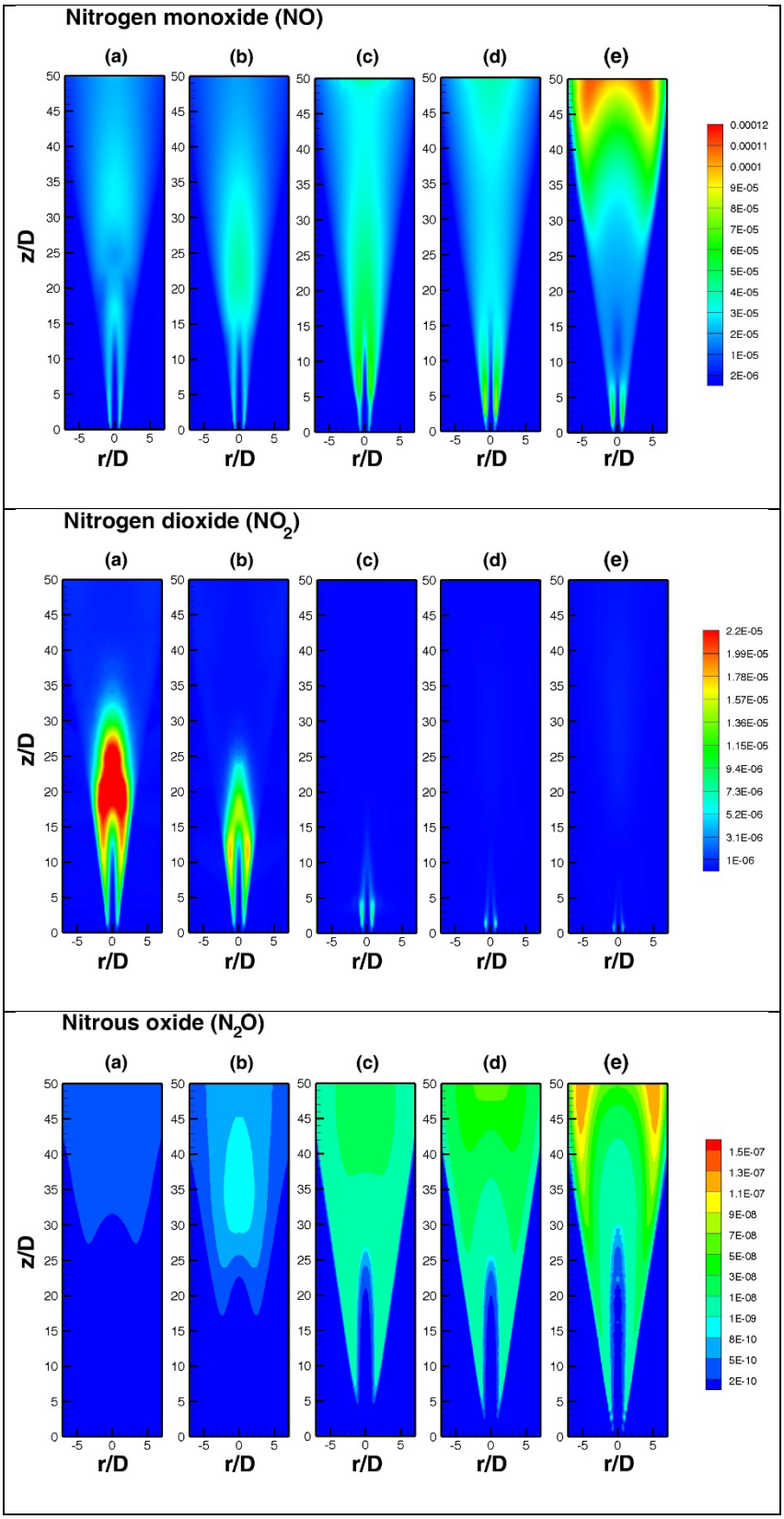
Nitrogen monoxide (NO)
(a)
(b)
(c)
(d)
(e)
z/D
r/D
0.00012
0.00011
0.0001
9E-05
8E-05
7E-05
6E-05
5E-05
4E-05
3E-05
2E-05
1E-05
2E-06
Nitrogen dioxide (NO2)
2.2E-05
1.99E-05
1.78E-05
1.57E-05
1.36E-05
1.15E-05
9.4E-06
7.3E-06
5.2E-06
3.1E-06
1E-06
Nitrous oxide (N2O)
1.5E-07
1.3E-07
1.1E-07
9E-08
7E-08
5E-08
3E-08
1E-08
1E-09
8E-10
5E-10
2E-10

Fig 15

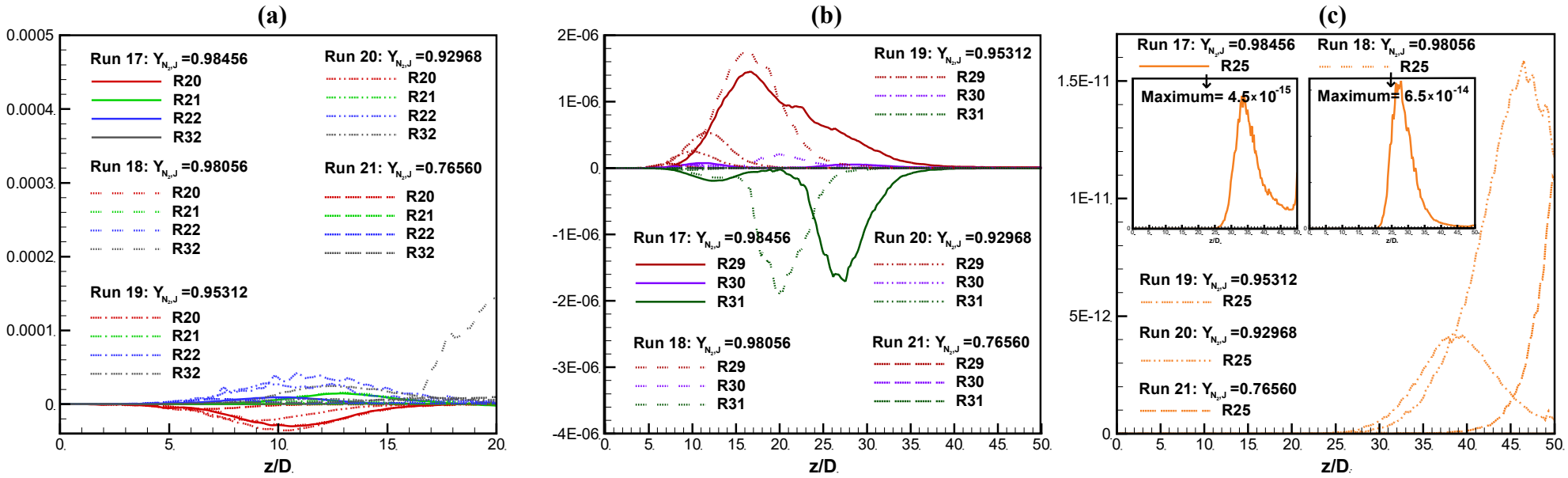
(a)
Run 17: $Y_{N_2,J}$ =0.98456
R20
R21
R22
R32
Run 20: $Y_{N_2,J}$ =0.92968
R20
R21
R22
R32
Run 18: $Y_{N_2,J}$ =0.98056
R20
R21
R22
R32
Run 21: $Y_{N_2,J}$ =0.76560
R20
R21
R22
R32
Run 19: $Y_{N_2,J}$ =0.95312
R20
R21
R22
R32
0.0005
0.0004
0.0003
0.0002
0.0001
0
0
5
10
15
20
z/D
(b)
Run 19: $Y_{N_2,J}$ =0.95312
R29
R30
R31
Run 17: $Y_{N_2,J}$ =0.98456
R29
R30
R31
Run 20: $Y_{N_2,J}$ =0.92968
R29
R30
R31
Run 18: $Y_{N_2,J}$ =0.98056
R29
R30
R31
Run 21: $Y_{N_2,J}$ =0.76560
R29
R30
R31
2E-06
1E-06
0
-1E-06
-2E-06
-3E-06
-4E-06
0
5
10
15
20
25
30
35
40
45
50
z/D
(c)
Run 17: $Y_{N_2,J}$ =0.98456
R25
Maximum= 4.5×10^{-15}
Run 18: $Y_{N_2,J}$ =0.98056
R25
Maximum= 6.5×10^{-14}
Run 19: $Y_{N_2,J}$ =0.95312
R25
Run 20: $Y_{N_2,J}$ =0.92968
R25
Run 21: $Y_{N_2,J}$ =0.76560
R25
1.5E-11
1E-11
5E-12
0
0
5
10
15
20
25
30
35
40
45
50
z/D

Fig 16

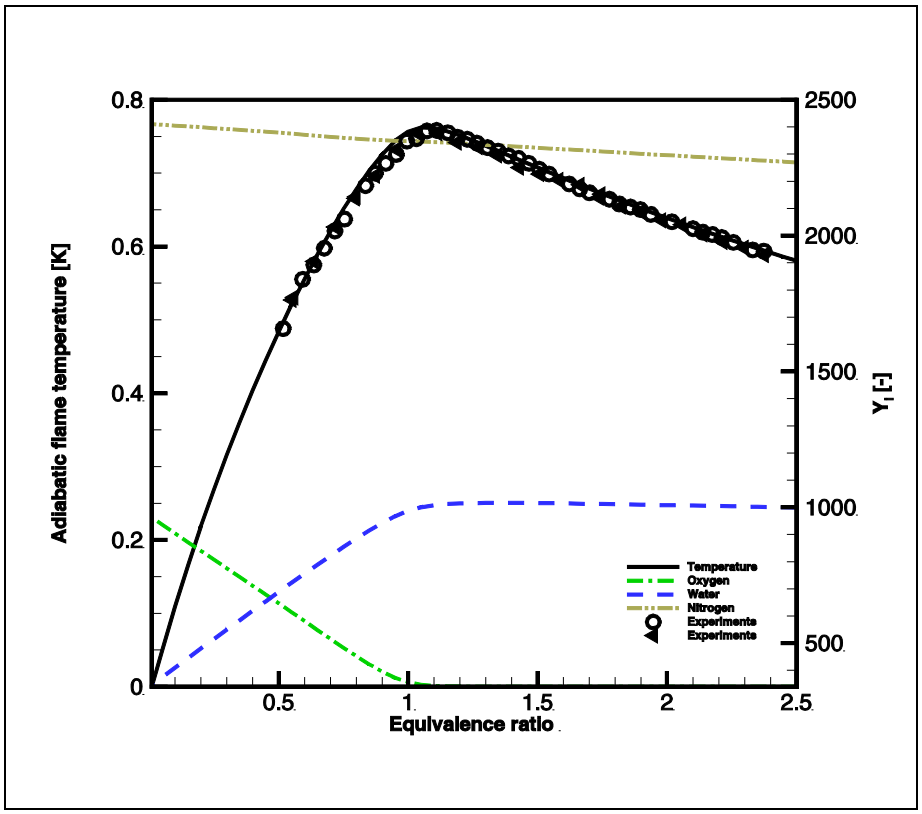
Adiabatic flame temperature [K]
0.8
0.6
0.4
0.2
0
2500
2000
1500
1000
500
Y_f [-]
0.5
1
1.5
2
2.5
Equivalence ratio
Temperature
Oxygen
Water
Nitrogen
Experiments
Experiments

Fig 17

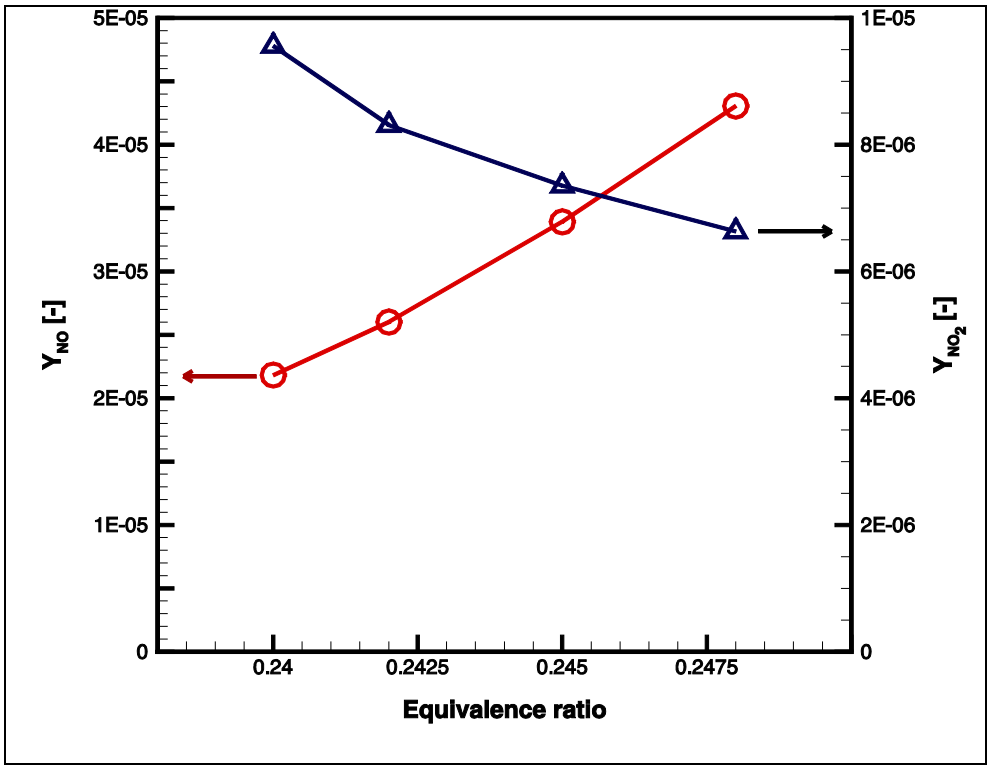
5E-05
4E-05
3E-05
2E-05
1E-05
0
Y_{NO} [-]
1E-05
8E-06
6E-06
4E-06
2E-06
0
Y_{NO_2} [-]
0.24
0.2425
0.245
0.2475
Equivalence ratio

Fig 18

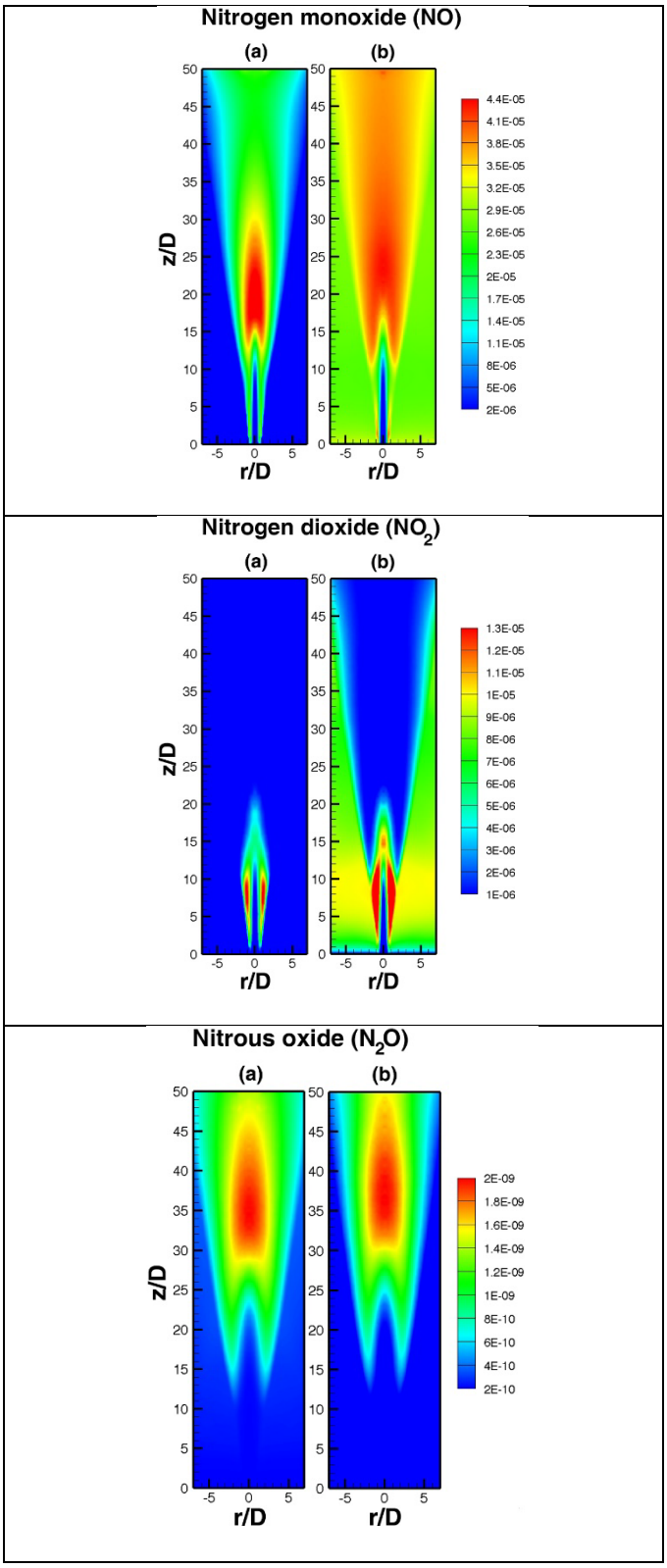
Nitrogen monoxide (NO)
(a)
(b)
z/D
r/D
4.4E-05
4.1E-05
3.8E-05
3.5E-05
3.2E-05
2.9E-05
2.6E-05
2.3E-05
2E-05
1.7E-05
1.4E-05
1.1E-05
8E-06
5E-06
2E-06
Nitrogen dioxide (NO2)
1.3E-05
1.2E-05
1.1E-05
1E-05
9E-06
8E-06
7E-06
6E-06
5E-06
4E-06
3E-06
2E-06
1E-06
Nitrous oxide (N2O)
2E-09
1.8E-09
1.6E-09
1.4E-09
1.2E-09
1E-09
8E-10
6E-10
4E-10
2E-10

Fig 19